Geochemistry, Geophysics, Geosystems

RESEARCH ARTICLE
10.1029/2019GC008648

Key Points:
- Thermal origin of density anomalies alone cannot explain observed geodynamic data
- Nonthermal density anomalies are found in the center of the large low-shear-velocity provinces
- Density models derived from joint inversion and from pure seismic inversion lead to different predicted mantle flow fields

Supporting Information:
- Supporting Information S1

Correspondence to:
C. Lu,
lcer.jsg@utexas.edu

Citation:
Lu, C., Forte, A. M., Simmons, N. A., Grand, S. P., Kajan, M. N., Lai, H., & Garnero, E. J. (2020). The sensitivity of joint inversions of seismic and geodynamic data to mantle viscosity. *Geochemistry, Geophysics, Geosystems*, *21*, e2019GC008648. https://doi.org/10.1029/2019GC008648

Received 21 AUG 2019
Accepted 31 MAR 2020
Accepted article online 6 APR 2020

The Sensitivity of Joint Inversions of Seismic and Geodynamic Data to Mantle Viscosity

Chang Lu[1], Alessandro M. Forte[2], Nathan A. Simmons[3], Stephen P. Grand[1], Marie N. Kajan[2], Hongyu Lai[4], and Edward J. Garnero[4]

[1]Department of Geological Sciences, Jackson School of Geosciences, The University of Texas at Austin, Austin, TX, USA, [2]Department of Geological Sciences, College of Liberal Arts and Sciences, University of Florida, Gainesville, FL, USA, [3]Atmospheric, Earth and Energy Division, Lawrence Livermore National Laboratory, Livermore, CA, USA, [4]School of Earth and Space Exploration, Arizona State University, Tempe, AZ, USA

Abstract Seismic tomography has revealed the existence of large-scale velocity heterogeneities in the mantle. The interpretation of seismic velocity anomalies in terms of temperature and chemical composition is nonunique. We use geodynamic observations including gravity, plate motions, dynamic topography, and excess ellipticity of the core-mantle boundary combined with seismic observations to investigate the thermo-chemical structure of the mantle through joint inversions. An outstanding issue, however, is the physical connection between mantle density anomalies and the surface geodynamic observations, which requires knowledge of the mantle viscosity structure. Here we perform joint inversions assuming different viscosity profiles and examine the dependence of the results on the viscosity. We first assume that mantle heterogeneity is due to thermal variations, which places a constraint on the relation between seismic velocity and density, and we subsequently relax the constraint to allow for potential nonthermal effects. In all of our joint inversions, a nonthermal origin of density anomalies is required to explain the geodynamic data, though the amount varies with the assumed viscosity structure. A common observation is a high-density chemical signal in the center of the large low-shear-velocity provinces at the base of the mantle resulting in a near neutral or slightly dense overall buoyancy there. Using the derived density models and their corresponding viscosity profiles, we also calculate instantaneous mantle flow fields. The predicted flow fields derived from joint inversions are generally similar but are quite different from flow fields using density models derived from a posteriori scaling of pure seismic tomography models.

Plain Language Summary The origin and evolution of Earth's mantle have been long-standing fundamental questions in geosciences. We use both global seismological and geodynamical (gravity, topography, plate motions, and excess ellipticity of the core-mantle boundary) data sets to investigate whether lateral changes in mantle structure can be explained solely by temperature variations or whether the mantle must also have significant chemical variations. Our results indicate the presence of chemically distinct mantle anomalies. In particular, we find two large regions at the base of the mantle that appear to be chemically distinct with hot mantle upwellings surrounding them. We also derived several models of 3D density variations in the mantle assuming different viscosity profiles. These models were then used to predict the present-day mantle convective flow. We show that the mantle viscosity structure does not have a strong influence on the pattern of large-scale mantle flow. We find, however, that 3D density models derived by simple (1D) a posteriori scaling of tomography models obtained only from seismic data yield predictions of significantly different mantle flow.

1. Introduction

Seismic tomography has shown that large-scale heterogeneity exists at all depths through the mantle (e.g., French & Romanowicz, 2014; Grand, 2002; Moulik & Ekström, 2016; Ritsema et al., 2011). However, the interpretation of these heterogeneities in terms of temperature and possible chemical variations is still debated. In the shallow mantle, it is well accepted that old, stable cratonic roots are compositionally distinct from surrounding mantle (Jordan, 1978). Excluding cratonic roots, there is controversy over whether thermal variations alone can explain the mantle heterogeneity or not. Most notably, the lower mantle is marked by two so-called large low-shear-velocity provinces (henceforth, LLSVPs) beneath the south-central Pacific and Africa (Garnero & McNamara, 2008) that have been the focus of debate over whether chemical or

thermal heterogeneity is dominant in these regions. Schuberth et al. (2009) and Davies et al. (2012) converted global mantle circulation models into elastic parameters and density and have suggested that substantial chemical heterogeneities are not necessary to explain lower mantle seismic anomalies, possibly owing to the limited resolution of seismic tomography. Opposing arguments for a dominantly chemical origin for the LLSVPs have been made based on the seismic inference of their sharp boundaries (e.g., Frost & Rost, 2014; Ni et al., 2002; Sun & Miller, 2013; Zhao et al., 2015), apparent anticorrelation of *S* wave and bulk sound velocities in the lowermost mantle (e.g., Forte & Mitrovica, 2001; Masters et al., 2000; Robertson & Woodhouse, 1996; Saltzer et al., 2001; Su & Dziewonski, 1997), geographical correlation of LLSVP edges in the deepest mantle with surface hotspots (e.g., Steinberger & Torsvik, 2012; Thorne et al., 2004), and source locations for large igneous provinces (e.g., Burke et al., 2008; Torsvik et al., 2010). The quantitative agreement between predicted entrainment of dense LLSVP material by plumes in ocean island basalt (Deschamps et al., 2011; Li et al., 2014) and the distinct isotopic ratios of elements compared with mid-ocean ridge basalts found in many hotspots (Hofmann & Hart, 1978) also supports a chemically distinct origin for the LLSVPs.

Constraining density perturbations, as well as seismic velocities, in the mantle is necessary to robustly discriminate between chemical and thermal anomalies. It is challenging, however, to use seismic data alone to determine density structure. Using normal mode splitting functions, Ishii and Tromp (1999) found anomalously high density within the African LLSVP implying that the mantle there is chemically distinct. Trampert et al. (2004) also showed chemically distinct LLSVPs using a probabilistic tomography method based on normal mode data. However, Kuo and Romanowicz (2002) found that the density structure retrieved from normal mode data was not reliable based on synthetic tests. Recently, Koelemeijer et al. (2017), using Stoneley modes, found the LLSVPs to be buoyant in contradiction with the results of Ishii and Tromp (1999). However, the recent work does not constrain the density in the lowermost 100 km of the mantle. Koelemeijer et al. (2017) also showed a trade-off between lowermost density structure and core-mantle boundary (CMB) tomography, which might bias the derived density structures. Other more recent work by Lau et al. (2017) again suggests overall dense LLSVPs through a method called "tidal tomography" using Earth's body tide data. Ding and Chao (2018) used excess density in LLSVPs to explain the correlation between the 6-year periodic variation in the length of the day and surface deformation. These apparent contradictions point to the continued uncertainty regarding the chemical contributions to these major, large-scale deep mantle anomalies.

An alternative approach to determine mantle density structure is to use geodynamic data such as Earth's gravity field, topography, and plate motions that provide direct constraints on mantle density anomalies. A direct theoretical relationship between these observables and mantle density structure can be established assuming a viscous flowing mantle with a known viscosity distribution (e.g., Forte & Peltier, 1987; Hager, 1984; Ricard et al., 1989). Therefore, a joint analysis of seismic and geodynamic data has the potential to discriminate thermal from chemical heterogeneity (e.g., Forte & Mitrovica, 2001; Trampert et al., 2004). Simmons et al. (2009, 2010) proposed a joint inversion method, where seismic, geodynamic, and mineral physics data are simultaneously inverted for temperature and chemical 3D structure. They initially build a relation, based on mineral physical constraints, between seismic velocity and density anomalies that assumes that the heterogeneity is due to thermal affects. Through joint inversion of the geodynamic and seismic data, a "thermal" model is found that best explains the data. In a second step, data that are not explained by the thermal model can be inverted for density anomalies that may not have a thermal origin. In this way, a model that simultaneously matches seismic and geodynamic constraints can be obtained with an estimate of the minimal chemical heterogeneity required to fit the data.

Given a mantle density structure, as well as a model of depth-dependent viscosity, the instantaneous flow of the mantle can be calculated (Forte, 2007; Hager & O'Connell, 1981; Steinberger, 1996). Assuming that subducting slabs are the main source of buoyancy in the mantle, mantle flow simulations have been done with dense lithospheric slabs providing all the driving forces (e.g., Gurnis, 1992; Lithgow-Bertelloni & Gurnis, 1997; Ricard et al., 1993). In other mantle convection studies, density models were derived by a posteriori scaling of seismic tomography using a radially varying or constant scaling factor between density and seismic velocity perturbations (e.g., Liu et al., 2008; Spasojevic et al., 2009; Steinberger, 2016). The predicted flow fields that result from these calculations can then be related to other independent geophysical and geological observations. For example, Becker et al. (2003), Conrad

et al. (2007), and Gaboret et al. (2003) computed flow models to predict mantle anisotropy that compared well with observations.

These mantle flow simulations have been used to better understand anomalous surface features of the Earth. For example, using their mantle flow simulations, Shephard et al. (2012) proposed that more than half of the anomalous depth of the Argentine Basin is caused by deep-seated mantle flow. Applying time-reversed convection simulations, one can also model the evolution of topography and tectonic processes through time (e.g., Bunge et al., 2003; Glišović & Forte, 2017; Liu et al., 2008; Moucha et al., 2008). However, different flow simulations can result in different conclusions related to surface evolution. For example, Rowley et al. (2013) determined that the east coast of the United States has undergone uplift over the past 3 Ma. They used the density model derived in Simmons et al. (2009) to drive flow simulations. In contrast, using a different mantle viscosity and density model and under different assumptions, Liu (2015) predicted subsidence of the same region over the same time period. As another example, Rowley et al. (2016) showed that a long-lived deep upwelling beneath the East Pacific Rise (EPR) drives horizontal asthenospheric flows away from the ridge and contributes significantly to plate motions through viscous traction, which challenges the traditional idea that slab pull is the dominant driving force of plate tectonics. In the flow modeling of Conrad and Behn (2010), however, deep mantle upwelling is focused further west than found by Rowley et al. (2016) and results in asthenospheric flow toward the ridge beneath parts of the west Pacific. Thus, in their model, asthenospheric flow works against plate motion, at least near the EPR.

The mantle flow models that resulted in contradictory conclusions, discussed above, use different viscosity and density models, thus obscuring a comprehension of the controlling factors yielding different results. In this study, we investigate the impact of assuming different geodynamically inferred 1D viscosity profiles on both mantle density estimation and mantle flow predictions. We use the approach of Simmons et al. (2009) to conduct joint inversions of seismic and geodynamic data to constrain mantle density perturbations assuming different viscosity models. The inversions find 3D density models that fit Earth's surface gravity field, topography, and plate motions, as well as minimizing the chemical heterogeneity within the mantle. Our goal is to test the sensitivity of the joint inversion results to the a priori choice of viscosity model. In particular, we test the extent to which the assumed viscosity structure influences inferences of chemical contributions to density heterogeneity and the corresponding predictions of instantaneous flow. In the following sections, we describe the data and method we use in the joint inversions; then, we discuss the effect of viscosity on the inferred thermal-chemical structure of the mantle. Finally, we compare the mantle flow predictions and evaluate the effect of viscosity structure on mantle flow patterns.

2. Data and Method

Our joint inversion follows the approach proposed by Simmons et al. (2009) to derive model TX2009 with some minor modifications to the method but with substantially expanded seismic data sets and geodynamic constraints. A two-step approach has been applied to simultaneously invert shear-wave seismic data and geodynamic data. First, we attempt to fit the data assuming that mantle heterogeneities have a thermal origin, thus applying simple scaling relationships between density and velocity perturbations based on mineral physical estimates. For each viscosity profile, we find the model yielding best data fit within plausible ranges of thermal density to velocity scaling. In the second step, we relax the purely thermal assumption and invert the geodynamic data for a total density model having both thermal and nonthermal origins. The difference between the total and thermal density fields yields a minimum estimate of the density variations with a nonthermal origin in the mantle.

2.1. Viscosity Profiles

Nonuniqueness of geodynamic constraints on mantle viscosity is manifested in a wide range of models that differ even in their 1D depth variation (e.g., Behn et al., 2004; Forte & Peltier, 1991; Forte & Peltier, 1987; Forte, Quéré, et al., 2010; Hager et al., 1985; Kido et al., 1998; King & Masters, 1992; Mitrovica & Forte, 2004; Panasyuk & Hager, 2000; Rudolph et al., 2015; Steinberger & Calderwood, 2006). In this study, we test five published viscosity models that have been widely used (Figure 1). The V1 viscosity profile was developed by Mitrovica and Forte (2004) by jointly inverting global convection-related data and glacial isostatic adjustment observations. The model is distinguished by a very low viscosity layer just above the 660-km discontinuity. Model V2 (Forte, Quéré, et al., 2010) was derived using a similar approach as V1

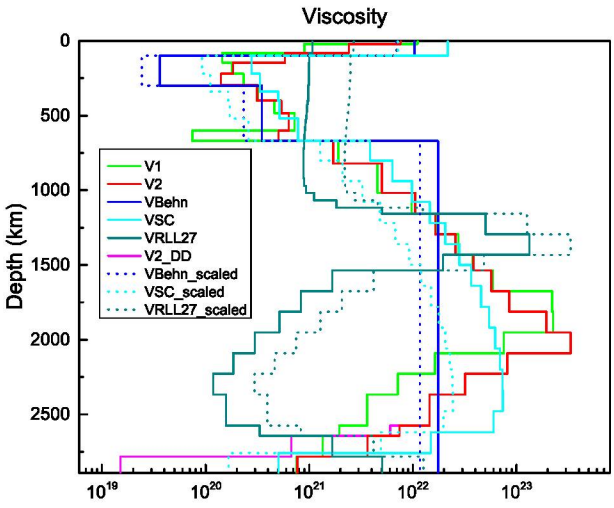

Figure 1. Radially symmetric viscosity models used in this study. Viscosity models used include V1 (Mitrovica & Forte, 2004) (green line), V2 (Forte et al., 2010) (red line), VBehn (Behn et al., 2004) (blue line), VSC (Steinberger & Calderwood, 2006) (cyan line), VRLL27 (Rudolf et al., 2015) (dark cyan line), and V2_DD (see main text) (magenta line). Dotted lines show scaled VBehn, VSC, and VRLL27 models, which aim to better fit present-day tectonic plate velocity data (see main text).

but imposing a smooth continuation of viscosity across the 660-km discontinuity. We also consider a four-layer model proposed by Behn et al. (2004) that we call VBehn. The VBehn model is marked by a thick asthenospheric layer with more strongly reduced viscosity than the other models and was derived by fitting tomography-based predictions of mantle-flow-induced seismic azimuthal anisotropy to observations of shear-wave splitting. A fourth model we use, VSC, is presented in Steinberger and Calderwood (2006). This model was used to match predictions of a tomography-based density model with constraints provided by the long wavelength nonhydrostatic geoid and by radial heat flux. The four viscosity models discussed above have similar features with a high-viscosity top layer (lithosphere), a low-viscosity upper mantle, and a higher average viscosity in the lower mantle. In detail, however, the models locally differ by more than an order of magnitude at a number of depths (Figure 1). As an example of a quite different viscosity model, we also test model VRLL27 from Rudolf et al. (2015). This model was derived using mineral physics-based calculations to determine a velocity-to-density relationship applied to a shear-wave tomography model to produce a 3D mantle density model. Viscosity was then determined by inverting for models that predict the geoid up to degree and order 7. This model is quite different from the others in that it does not have a high-viscosity lithospheric layer and the viscosity in the lower half of the mantle is quite low. It is marked by a high-viscosity layer from about 1,000- to 1,500-km depth. Previous studies suggest that the existence of post-perovskite (pPv) can reduce viscosity at the bottom of the mantle and has a large impact on mantle convection (e.g., Deschamps & Li, 2019; Nakagawa & Tackley, 2011). To investigate the effect of low viscosity in D″, we use a sixth viscosity model, V2_DD, obtained by modifying viscosity model V2 such that it has a three-order of magnitude drop in viscosity in the bottom 300 km of the mantle.

2.2. Geodynamic Constraints

The geodynamic observations used in this study include the Earth's free-air gravity field, present-day tectonic plate divergence, dynamic surface topography, and excess CMB ellipticity. The free-air gravity field was derived from GRACE satellite data (Tapley et al., 2007). The rate of horizontal divergence of the tectonic plate velocities was obtained from the GEODVEL model in the no-net-rotation frame of reference (Argus et al. (2010)). Forte and Peltier (1994) have shown that a scalar representation of the plate velocity field in terms of its horizontal divergence provides a complete description of surface kinematics assuming that the plates are rigid bodies moving in a no-net-rotation reference frame. The dynamic surface topography was inferred by removing all isostatic crustal contributions (including water, ice, and sediments) to Earth's observed surface topography (Forte & Perry, 2000; Forte et al., 1993). These data are the least robust in our geodynamic observations because of the uncertainties in the crust model. Here we employ the crustal correction for surface topography based on model ETOPO1 (Amante & Eakins, 2009) and CRUST1.0 (Laske et al., 2013), whereas an older model CRUST2.0 (Bassin et al., 2000) was used in the derivation of TX2009. The three geodynamic data sets discussed above have been expanded up to spherical harmonic degree 32, whereas a degree-16 representation of the geodynamic data was used in previous joint inversions (Simmons et al., 2009, 2010). In addition, the excess ellipticity of the CMB (an excess flattening of 400 m) inferred from studies of the Earth's free-core nutation is also included (Herring et al., 2002; Mathews et al., 2002). This CMB topography constraint is represented by a single degree-2 zonal harmonic. Although we only use a single harmonic as a constraint on CMB topography, our inversions yield predictions of CMB topography up to degree and order 32 that are dynamically consistent with the mantle density and flow resulting from the inversions discussed below. Although the excess flattening constraint is not from a direct measurement of the CMB topography, the different VLBI inferences of excess ellipticity have yielded consistent estimates (e.g., Dehant et al., 2017). We thus feel, given the dynamical significance of this constraints, that its use is justified in the derivation of more realistic mantle density models.

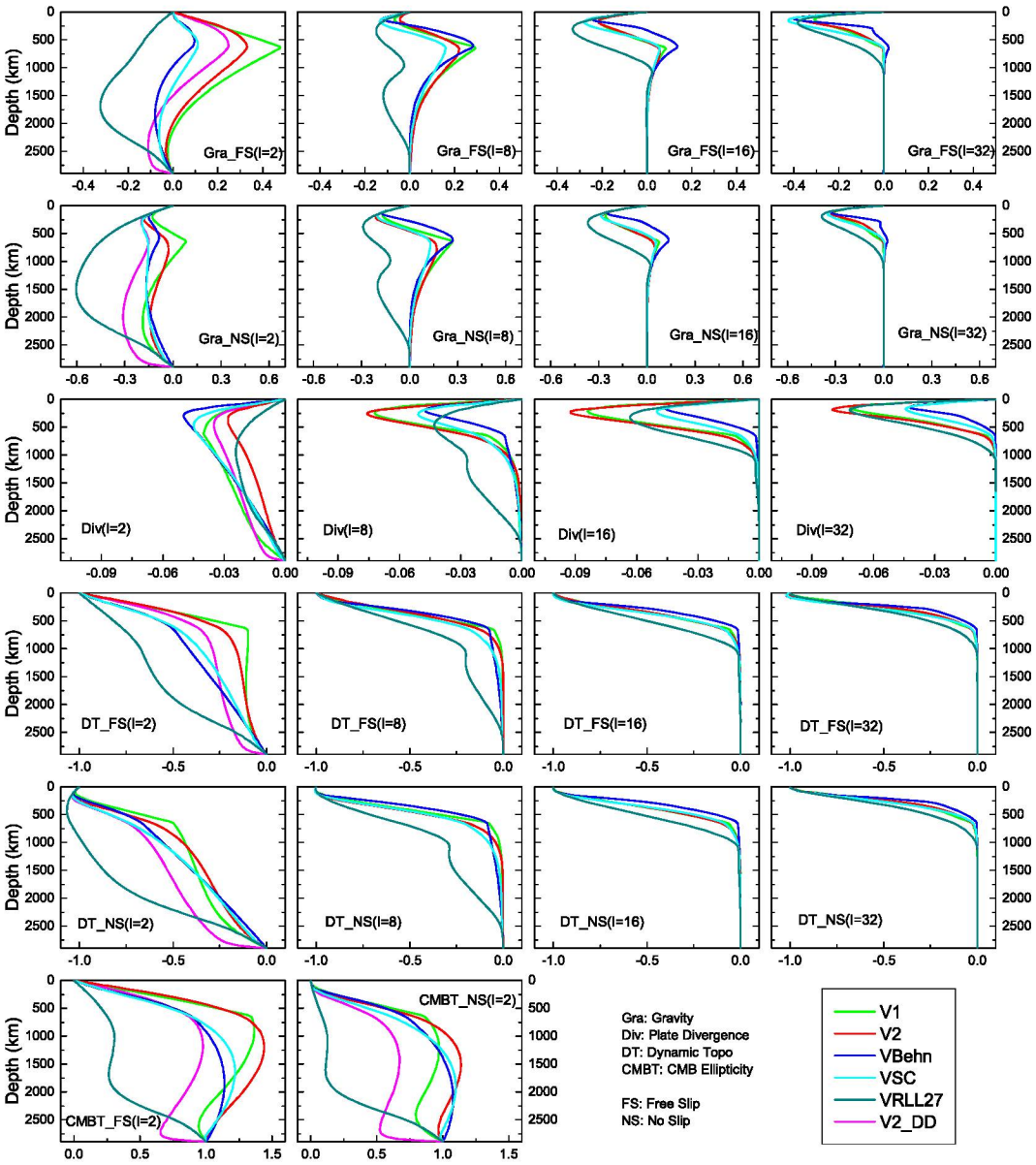

Figure 2. Geodynamic sensitivity kernels as a function of depth for viscosity profiles used in this study at representative spherical harmonic degrees. The colors of the lines correspond to different viscosity models. The type of geodynamic data, the boundary condition used in the kernel calculation, and the spherical harmonic degree are as labeled in each plot (see explanatory legend at the bottom of the figure). Plate motion kernels for "VBehn," "VSC," and "VRLL27" models have been scaled as described in the text.

Assuming a compressible and gravitationally consistent mantle, the sensitivity kernels of these data were computed as the theoretical linear relationship between the surface observables and lateral density variations at different depths in the mantle (see Forte, 2007; Forte et al., 2015, for detailed derivations). The surface tectonic plates are viscously coupled to (and driven by) the underlying buoyancy-driven mantle flow (Forte & Peltier, 1991, 1994). A combined free-slip and no-slip surface boundary condition was applied in the kernel calculation (Forte, 2007) to account for plate-like character of the surface boundary, resulting in cross-mode coupling of all harmonic components of the mantle flow field (Forte & Peltier, 1994). The geodynamic sensitivity kernels for each viscosity profile at selected spherical harmonic degrees are shown in Figure 2. Different viscosity profiles lead to different sensitivity kernels, especially at the longer wavelengths. These differences motivate our investigation of the impact of a priori assumptions about viscosity on joint tomography inversions and mantle flow predictions.

The sensitivity kernels for gravity and topography are not sensitive to absolute viscosity but only the relative viscosity variation with depth (Forte, 2007). Plate motions, however, are sensitive to the absolute viscosity. To ensure no baseline (i.e., mean absolute viscosity) bias in comparing viscosity models, we first used the 3D density model from Simmons et al. (2010) to compute plate motions predicted by the six viscosity models discussed above. We found that viscosity models VBehn and VSC underpredicted the velocity of plates (i.e., the overall viscosities were too stiff). We therefore scaled model VBehn by .67 and model VSC by .33 to best match the plate motions. Model VRLL27 actually predicted plate motions that were too fast, so we increased the viscosity by a factor of 2.5 to match the speed of plates (Figure 1). Viscosity models V1, V2, and V2_DD were not scaled as they were derived using plate motions as input and the same theory as used here. The geodynamic kernels shown in Figure 2 were computed using the scaled versions of viscosity models VBehn, VSC, and VRLL27 shown in Figure 1.

2.3. Seismic Constraints

We include two groups of shear-wave seismic data in our joint inversions. The first group is the same data set we used in our previous global tomography studies (Lu & Grand, 2016), which is an extended version of the seismic data used in TX2009 (Simmons et al., 2009). These seismic data consist of ~70,000 global S, ScS, SKS, and SKKS phase traveltimes, as well as their surface bounce equivalents (SS, S3, S4, ScS2, ScS3) and their upgoing wave equivalents (sS, sSS, sS3, sS4, sScS2, sScS3) from 540 earthquakes. Upper-mantle triplicated waves are also included that provide resolution of structure in the transition zone, which is geodynamically significant (Figure 2). Grand (1994) presents a complete discussion of how the shallow turning waves were analyzed. The data were corrected for variations in crustal thickness using model CRUST1.0 (Laske et al., 2013). The other group of shear-wave data is taken from Lai et al. (2019). They used a semiautomated procedure to measure the onset times of horizontally polarized S, SS, SSS, ScS, and ScSScS waves produced by 360 earthquakes. The data only include waves that turn in the lower mantle, so these data provide limited resolution of upper mantle structure. The measurement process involved the derivation of an empirical wavelet, which matched the seismic waveforms, through an iterative cross-correlation process. The onset times were measured on the basis of a Gaussian function, which best fit the empirical wavelet resulting in a total of about 226,000 seismic traveltime measurements. Details of the measurement process can be found in Lai et al. (2019). The seismic sensitivity kernels for both groups of data were calculated using 1D ray tracing (infinite frequency approximation). Since the Lai et al. (2019) data specifically measured onset times and the first data set examined the initial parts of waveforms bandpassed from .08 to .01 Hz, finite frequency effects are less important for these data compared to lower frequency data typically used in global shear-wave tomography. For all the seismic data, the 1D velocity model used in Grand (1994) is used as the reference model.

2.4. Mineral Physics Scaling Factor

In this paper, we jointly invert seismic and geodynamic data. This requires some relationship between seismic heterogeneity and density heterogeneity. To make the inversions linear, we must assume a linear relationship between the two. Then, the relationship between density and shear-wave velocity perturbations can be represented by a scaling factor $R_{\rho/Vs}$, which is the ratio of density to velocity heterogeneity defined by

$$R_{\rho/V_S} = \frac{dln\ \rho}{dlnV_S}. \tag{1}$$

Assuming that mantle heterogeneities have a thermal origin, a depth-dependent $R_{\rho/Vs}$ can be obtained by extrapolating high-pressure, high-temperature mineral physics measurements for a given mantle chemical composition along a geotherm. The scaling factor $R_{\rho/Vs}$ here includes both anharmonic and anelastic contributions (Karato & Karki, 2001). In the derivation of TX2009, the scaling factors were taken from estimates made by Cammarano et al. (2003) for the upper mantle and Karato and Karki (2001) for the lower mantle. Here we derive new scaling factors using updated mineral physics data. A complete discussion of our method is given in the supporting information.

Table S1 summarizes the mineral physics data we used (Anderson & Isaak, 1995; Duffy & Anderson, 1989; Fei, 1995; Finger & Ohashi, 1976; Fiquet et al., 2000; Flesch et al., 1998; Isaak, 1992; Jackson et al., 2003;

Jackson et al., 2007; Kung et al., 2005; Li & Neuville, 2010; Liu et al., 2009; Lu et al., 2013; Murakami et al., 2007; Murakami et al., 2012; Sinogeikin & Bass, 2002a, 2002b; Sinogeikin et al., 2003; Suzuki et al., 1980; Yang et al., 2016; Zha et al., 1998). We assumed a "pyrolite" mantle mineral assemblage (Stixrude & Lithgow-Bertelloni, 2012) and randomly perturbed all the thermoelastic data we selected within their estimated uncertainties. In this exercise we did not include the pPv phase. For each realization of the mineral physics measurements, we computed the depth-dependent anharmonic (elastic) scaling factors $R^{el}_{\rho/Vs}$ (Birch, 1978; Hill, 1952). The details of the calculations are given in the supporting information and follow the procedure given in Lu et al. (2013). We obtained over 10,000 anharmonic scaling factors $R^{el}_{\rho/Vs}$ at each depth along a 1,600-K adiabatic geotherm (Katsura et al., 2010). We use the ensemble mean values as the starting scaling factors in our inversions and $\pm 2\sigma$ (corresponding to 95.4% confidence intervals) define their uncertainties.

Anelasticity is known to have a significant effect on the temperature derivative of shear-wave velocity and thus the scaling factor $R_{\rho/Vs}$ throughout the mantle (Cammarano et al., 2003; Karato & Karki, 2001). The effect of anelasticity on the temperature derivative of shear velocity can be written as follows:

$$\left(\frac{\partial lnV_S}{\partial T}\right)_{anel} = \left(\frac{\partial lnV_S}{\partial T}\right)_{el} - \frac{1}{\pi}\frac{F(\alpha)}{Q_S}\frac{E^* + PV^*}{RT^2}, \tag{2}$$

$$F = \frac{\alpha\pi}{2}\, cot\frac{\alpha\pi}{2}, \tag{3}$$

where α is a phenomenological material-dependent constant that represents the frequency dependence of attenuation, E^* is the activation energy, V^* is the activation volume, R is the universal gas constant, T is temperature, and P is pressure. The subscripts *el* and *anel* denote the purely elastic derivative and the total temperature derivative after adding the anelastic effect, respectively. The shear-wave quality factor Q_S can be expressed as follows:

$$Q_S = Q_0\omega^{\alpha}\exp\left(\frac{\alpha E^* + \alpha PV^*}{RT}\right), \tag{4}$$

where ω is angular frequency and Q_0 is a constant that can be derived if average seismic observed Q (Anderson & Hart, 1978; Durek & Ekström, 1996; Dziewonski & Anderson, 1981; Hwang & Ritsema, 2011; Lawrence & Wysession, 2006; Montagner & Kennett, 1996; Widmer et al., 1991) and lateral temperature variations at given depth are known. Here we adopted the method proposed by Matas and Bukowinski (2007) to constrain Q_0 and corrected for the anelasticity effect on $R_{\rho/Vs}$ (see supporting information for details). We again perturb the above anelastic parameters randomly within their plausible ranges to estimate the uncertainties of scaling factor at each depth (Table S2). After adding the anelastic contribution, our 1D scaling factor is generally consistent with previous studies though there are differences at particular depths (Cammarano et al., 2003; Karato & Karki, 2001; Steinberger & Calderwood, 2006) (Figure 3). The combined anharmonic and anelastic thermal scaling factors discussed above were used as a starting model in the inversions discussed below.

3. Inversion

Given a relation between seismic velocity and density anomalies, the seismic and geodynamic data can be inverted simultaneously. We follow Simmons et al. (2009) and parameterize the velocity and density perturbations in the mantle by a set of blocks approximately 275 × 275 km in lateral dimension and thickness varying from 75 to 240 km in the radial direction with thicker blocks in the bottom of the mantle. Following Lu & Grand (2016), we also simultaneously invert for earthquake location in the joint inversion. The combined linear seismic-geodynamic system of equations can then be represented by the following equation:

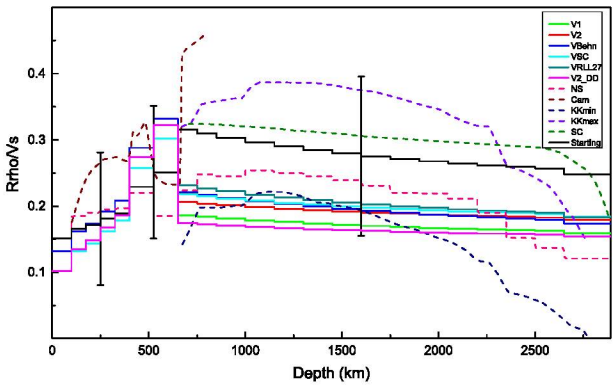

Figure 3. Shear-wave velocity-to-density scaling profiles as a function of depth. The starting scaling factor with estimated uncertainties at representative depths (black solid line) and optimal scaling factors for each viscosity model determined from grid search (colored solid lines) are compared with mineral physics predictions (dash lines). "KKmax" and "KKmin" are maximum and minimum values, respectively, predicted by Karato and Karki (2001). The other mineral physics-derived scaling factors, including "Cam" (Cammarano et al., 2003), "SC" (Steinberger & Calderwood, 2006), and optimal scaling factor "NS" determined in a previous joint inversion (Simmons et al., 2009), are also shown for comparison.

$$\begin{bmatrix} L & A \\ \lambda_G G(R_{\rho/V_S}, -V_S) & 0 \\ \lambda_c c(R_{\rho/V_S}, -V_S) & 0 \\ \lambda_D D & 0 \end{bmatrix} \begin{bmatrix} \Delta m \\ \Delta q \end{bmatrix} = \begin{bmatrix} r_S \\ \lambda_G g \\ \lambda_c e \\ 0 \end{bmatrix}, \quad (5)$$

where Δm is the seismic slowness perturbation relative to the reference 1D velocity model, L is the seismic sensitivity matrix, and r_S is the shear-wave traveltime data. G and g represent the viscous flow sensitivity kernels and data where each row corresponds to a specific spherical harmonic component of the free-air gravity, plate divergence, and surface dynamic topography. The row-vector c is the sensitivity function corresponding to the degree-2 zonal harmonic coefficient representing the excess ellipticity of the CMB. The observed ~400-m excess ellipticity is represented here by the scalar quantity e. The spherical harmonic geodynamic sensitivity kernels have been integrated into the blocks as in Simmons et al. (2009). Matrix D is a second-order digital smoothing filter with 76% of the weight applied to the lateral blocks and 24% of the weight applied in the radial direction. The λ terms are scalar weighting factors that weight different observations. R_{ρ/V_S} represents the linearized relationship between density perturbations (ρ) and shear-wave velocity (Vs) perturbations. A reference 1D shear-wave velocity (V_S) model is also needed in the conversion since we invert for slowness perturbation Δm. Vector Δq contains the perturbations to the earthquake latitude, longitude, depth, and origin time for each earthquake, and A represents the partial derivatives of these parameters. We used the least-squares method (Paige & Saunders, 1982) to solve equation 5 for a number of inversions as discussed below.

The inversion involves several different weighting factors that are critical in terms of the resulting models. λ_D controls the trade-off between minimizing model roughness and minimizing data misfit. We followed Lu and Grand (2016) and performed a standard L-curve analysis just using the seismic data. The trade-off between roughness and data fit has a corner point for λ_D of about 2,600, and we use that value in most of the following inversions. The weights of the geodynamic data (λ_G and λc) are also important for the joint inversions. Using our best estimate for the scaling factor $R_{\rho/Vs}$, we conducted a series of joint inversions to determine the optimal weights. Figure 4 shows the variance reductions for the seismic and geodynamic data as we increase the weight of the geodynamic data. Variance reduction for the geodynamic data is defined as follows:

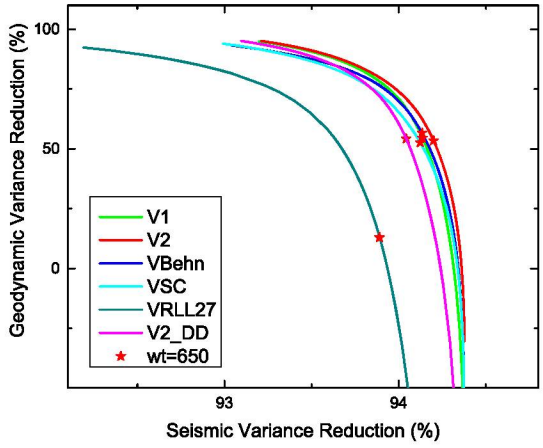

Figure 4. Trade-off curves between seismic and geodynamic variance reductions for different viscosity models. As the weight for geodynamic data increases in the joint inversion, seismic variance reduction decreases while geodynamic variance reduction increases. We chose a weight of 650 near the corner points in the L curves for viscosity models V1, V2, VBehn, VSC, and V2_DD. The red stars show the geodynamic and seismic variance reductions for this weight.

$$VR = \left[1 - \frac{\sum_l \sum_{m=-l}^{+l} (O-P)_l^{m*} (O-P)_l^m}{\sum_l \sum_{m=-l}^{+l} O_l^{m*} O_l^m}\right] \times 100\%, \quad (6)$$

where O and P are the complex harmonic coefficients of the observed and predicted fields, respectively, and * denotes complex conjugation.

When the geodynamic data have zero weight (i.e., using a pure seismic model), there is a very poor fit to the geodynamic data with overall negative variance reduction for many observations (Figure 4; Table 1). This is true for all the viscosity models. With increasing weight given to the geodynamic data, there is a significant increase in fit to the geodynamic data without much degradation to the seismic data. There is a clear corner point, after which increasing the weight of the geodynamic data does begin to degrade the fit to the seismic data. We chose 650 for λ_G as our optimal weight for all the viscosity models, which is close to the corner points for all the viscosity models (Figure 4). The excess CMB ellipticity

is one of the strongest and most robust geodynamic constraints on integrated buoyancy in the deepest mantle, and we therefore chose a large weight (2,000) for λc in equation 5.

Figure 4 shows that there is still significant misfit of the geodynamic data after joint inversion for all the viscosity models using our best guess for linear thermal scaling between velocity and density perturbations. The misfit may be due to chemical variations in the mantle or other factors we have not accounted for, but we take a more conservative approach here and assume that the thermal velocity-to-density relation can be improved. This is reasonable given the large uncertainties in the mineral physics parameters, particularly for the anelastic effects. We performed a grid search of optimal scaling factor within its plausible range for each viscosity model we tested. To make the grid search feasible, we adopted the approach of Simmons et al. (2010) and defined the scaling factor as follows:

$$R_{\rho/V_S} = aR^{start}_{\rho/V_S} + b, \tag{7}$$

where a represents a multiplicative change in our best estimate 1D scaling factor and b is the corresponding baseline shift. For the upper and lower mantle, we defined two sets of coefficients due to the possibility of large differences between them.

Simmons et al. (2009) have shown that in order to obtain adequate fits to geodynamic data, a simple 1D linear scaling factor $R_{\rho/Vs}$ was not sufficient to account for the relative behavior of density and S wave velocity. The long hypothesized existence of compositionally distinct cratonic keels and the temperature dependence of attenuation are possible reasons for this. In order to account for these two effects, they introduced a linearized correction factor to the scaling factor, which can be rewritten as follows:

$$R_{\rho/V_S} = aR^{start}_{\rho/V_S} + b + \varepsilon\, \delta \ln V_S, \tag{8}$$

where ε is the correction factor and δlnV_S represents the shear-wave perturbation we derived using seismic data alone. We adopted this approach and included these corrections in our grid search. In total, three correction factors were considered, including one for craton regions down to 250-km depth, one for noncraton regions from the surface to 250-km depth, and another one for the rest of the upper mantle and transition zone. The correction factor for cratons is expected to be negative since we expect smaller $R_{\rho/Vs}$ in fast velocity cratonic regions due to iron depletion (Forte & Perry, 2000; Jordan, 1978). In low-velocity noncratonic upper mantle, the correction factor is expected to be a positive value to reduce $R_{\rho/Vs}$ in hotter regions, in agreement with the predicted behavior due to the temperature dependence of Q_S.

We therefore have seven unknown parameters to be constrained in the grid search for each joint inversion. For each set of parameters, one joint inversion is required. In order to save computation cost, we searched for upper-mantle and lower-mantle parameters separately. We fixed lower-mantle $R_{\rho/Vs}$ and searched for the best fit upper-mantle parameters, then fixed the updated upper-mantle $R_{\rho/Vs}$, and searched for optimal lower-mantle parameters. After a few iterations, searching separately for upper-mantle and lower-mantle parameters, the search converged, and we obtained the best fit 1D scaling factor and three correction factors in the upper mantle for each viscosity profile. The optimal scaling factors show similar trends for the different viscosity profiles (Figure 3). In the upper mantle, the joint inversions prefer a lower scaling factor at shallow depths and higher values in the transition zone. In the lower mantle, the best fit scaling factor from equation 7 moves to the lower bound in our mineral physics estimation. Also, we found less variation with depth for the scaling factor in the lower mantle compared with the starting model, which agrees with the observation by Simmons et al. (2010).

3.1. Thermal Inversion

Using the optimal 1D scaling factor with the three correction factors (equation 8), the joint inversion provides mantle density models for each viscosity profile. We call these models "thermal models" although we use a different scaling for cratonic lithosphere implying chemically distinct cratonic keels. The variance reductions of seismic and geodynamic data for each density model are summarized in Table 1. The differences between the seismic models derived by joint inversion and pure seismic inversion results are visually small as seen in Figure S6. However, the derived density models from joint inversions yield significantly higher variance reduction of geodynamic constraints. The V1 model yields the highest overall variance reduction among

Table 1
Variance Reduction Results for Derived Models[a]

		V1	V2	VBehn	VSC	VRLL27	V2_DD
Seismic data (%)[b]		94.3	94.3	94.2	94.2	94.0	94.3
Gra (%)	Seismic + R_{ρ/V_S}^{start} [c]	−125.2	−65.8	−86.1	−77.3	−1,805.8	−437.5
	Thermal density	42.5	32.0	40.3	30.8	−121.1	30.9
	Total density	93.6	91.8	80.4	82.7	64.7	91.8
Div (%)	Seismic + R_{ρ/V_S}^{start}	−117.9	−12.3	49.0[c]	50.7	−63.3	−112.6
	Thermal density	80.7	80.0	75.4	80.7	85.0	83.5
	Total density	99.7	99.6	96.0	97.8	96.2	99.7
DT[d] (%)	Seismic + R_{ρ/V_S}^{start}	−19.3	−14.4	−31.3	−46.4	−301.5	−122.9
	Thermal density	52.8	50.0	46.9	53.4	48.6	53.7
	Total density	80.1	79.2	71.2	71.8	74.1	80.0
CMBT[e] (%)	Seismic + R_{ρ/V_S}^{start}	112.0	166.4	256.2	250.4	213.1	44.7
	Thermal density	8.7	8.1	20.9	23.6	13.2	9.5
	Total density	1.2	0.5	1.6	0.2	1.0	0.2

[a]Velocity model derived in joint inversion is used to check the seismic data fit, while density models are used to check the geodynamic data fit (Gra: free-air gravity, Div: plate divergence, DT: dynamic topography, CMBT: excess CMB ellipticity). [b]Scaled pure seismic model using starting scaling factor. [c]Unscaled VBehn, VSC, and VRLL27 models are used to check plate divergence fit. [d]CMBT is in percentage error. [e]Velocity model derived from pure seismic inversion yields 94.4% variance reduction.

all the viscosity models we tested, while model VRLL27 is unable to fit the gravity data, unlike the other five viscosity models. The joint inversions assume that mantle heterogeneity, outside cratonic regions, has a thermal origin, which might not be the case in the Earth. In fact, there remain significant misfits to the geodynamic data for all the viscosity models, implying that more complex models are required to fully reconcile the seismic and geodynamic data constraints on 3D mantle heterogeneity.

3.2. Nonthermal Inversion

There are several possible mineral physical reasons for the outstanding misfits to the geodynamic data after joint inversion, including (1) lateral variations of composition in noncratonic regions; (2) partial melting; and (3) a more complex behavior of thermal scaling factor than in our equation 8. All these possibilities will be referred to as "nonthermal" effects in the following discussions. In order to estimate the "nonthermal" effects, we fix the velocity models from the preceding thermal inversions and invert for a 3D scaling factor between seismic velocity and density as follows:

$$\begin{bmatrix} \lambda_G G(\Delta m) \\ \lambda_c c(\Delta m) \\ \lambda_D' D \end{bmatrix} \Delta R_{\rho/V_S}^{3D} = \begin{bmatrix} \lambda_G g \\ \lambda_c e \\ 0 \end{bmatrix}. \tag{9}$$

We call the density models obtained using the derived 3D scaling factors "total density" models since they represent all the mantle density anomalies required to fit the geodynamic observations that include both thermal and nonthermal contributions. The smoothing weight λ_D' is determined through a trial-and-error process to make the roughness of the "total density" model the same as the corresponding "thermal density" model. The difference between the "total density" and "thermal density" models gives the density anomalies caused by "nonthermal" effects. After the nonthermal inversion, the "total density" models derived using different viscosity profiles yield very good geodynamic data fits (Table 1), up to spherical harmonic degree 32, with variance reductions over 60% and most over 70%. The gravity field is fit with a variance reduction of over 80% for each viscosity model except for model VRLL27, which has a variance reduction of 64.7%. For the other geodynamic observables, variance reductions of 70% are achieved for all the viscosity models.

4. Mantle Heterogeneity Models

4.1. Thermal and Nonthermal Contributions

Figure 5 plots the distribution of derived 3D scaling factors for each viscosity model. The 3D scaling factors vary the most in the shallow and deepest mantle. We note, in particular, that viscosity models V1, V2, and

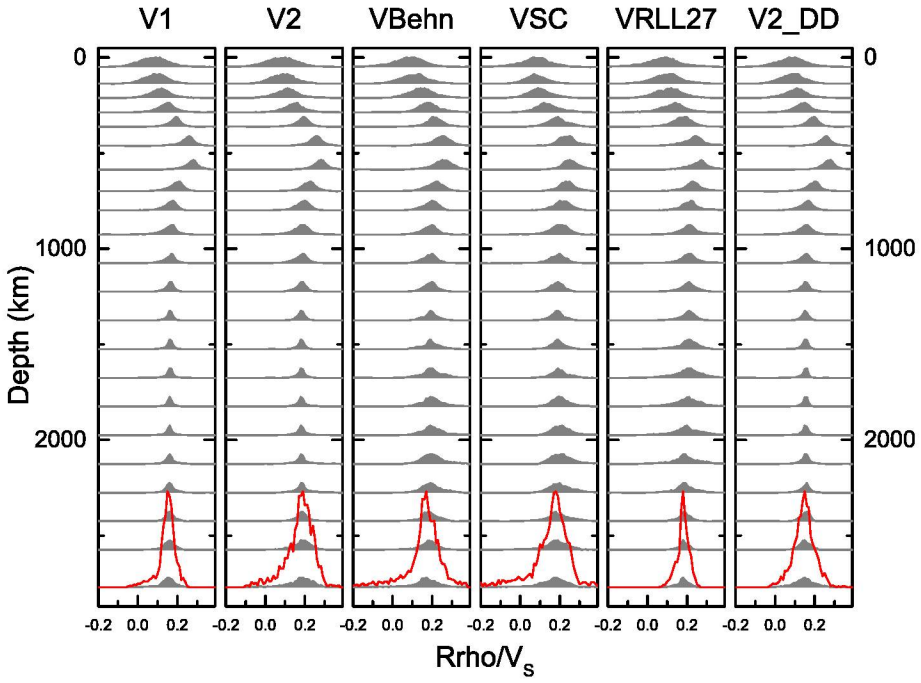

Figure 5. Distributions of derived 3D scaling factor from nonthermal inversion. The red lines are the zoomed-in plots to better illustrate the distribution above CMB.

V2_DD yield the smallest lateral variations in most of the lower mantle. Figures 6 to 10 show the density anomalies produced by our inversions for each viscosity model. In each figure, the left column displays density anomalies from the joint inversions using the optimized thermal scaling factors described by equation 8. The middle column shows the density anomalies that we call nonthermal and further including the density anomalies in cratonic keels that are due to differences in their chemical composition relative to the surrounding upper mantle. The column on the right shows the combined or total density models due to thermal and nonthermal variations. The density models using different viscosity profiles show similar large-scale features. The whole-mantle average correlation coefficients between the V1 thermal density model and the models using V2, VBehn, VSC, VRLL27, and V2_DD are 0.99, 0.97, 0.97, 0.91, and 0.99, respectively. In the case of the "thermal density" models, dense cratons and buoyant spreading centers are seen in all five models at 100- to 175-km depth, but their amplitudes vary slightly (Figure 6). In this depth range below the EPR, model VBehn has the most positive buoyancy while it is least buoyant in model VSC. Dense materials are detected under major subduction zones in all five models inside the transition zone (Figure 7). In the midlower mantle (Figures 8 and 9), all the "thermal density" models have elongated positive density anomalies beneath southwestern Eurasia and North America, which are believed to be related to ancient subduction of the Tethyan and Farallon slabs, respectively. In the same depth ranges, negative density anomalies are seen beneath southern Africa and the central Pacific. At the bottom of the lower mantle (Figure 10), all the "thermal density" models show the existence of two large-scale buoyant LLSVPs, but again, the amplitude of the anomalies varies among the models.

In general, the amplitudes of the nonthermal density anomalies are smaller than the thermal density anomalies throughout most of the mantle for all the models. Figure S7 shows the ratio of root-mean-square nonthermal density anomalies to the root mean square of the total density field as a function of depth for the different viscosity models. For all the viscosity models, nonthermal (chemical) variations are strong in the upper 300 km and lower 300 km of the mantle with little nonthermal density variation needed in the mantle between. In contrast, viscosity model VRLL27 requires comparatively more nonthermal density anomalies through the bulk of the mantle, while requiring the least nonthermal contributions in the lowermost 300 km of the mantle. We reiterate here that our modeling approach finds models

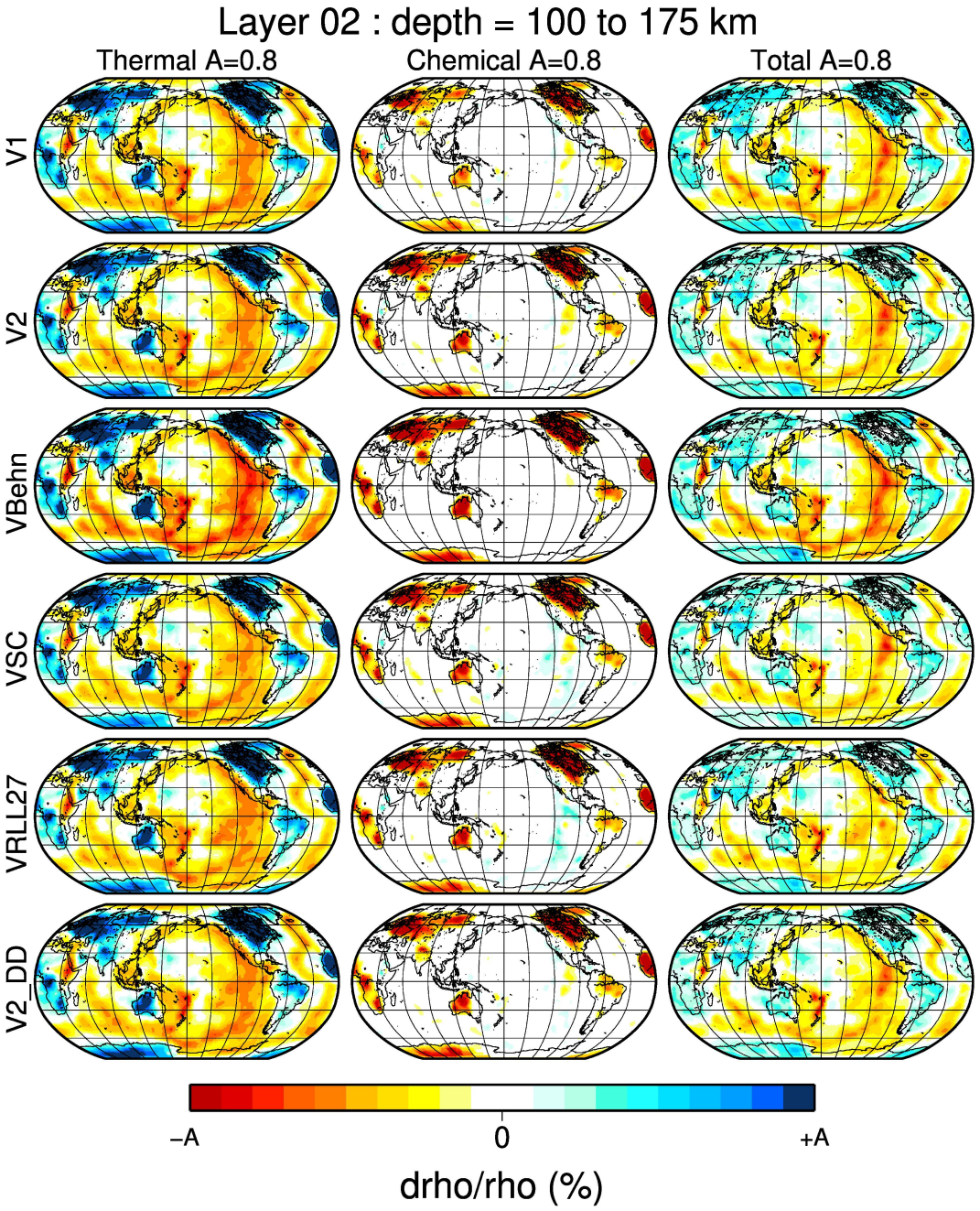

Figure 6. Lateral density variations derived from joint inversions between 100- and 175-km depth. Each row corresponds to a particular viscosity model used in the joint inversion, and the three columns correspond to each component of the density perturbation. Left column shows thermally induced density models obtained using the corrected 1D optimal scaling factor in joint inversion. Right column shows the total density models derived by letting the scaling factor vary in 3D to best fit the geodynamic data while keeping the velocity model fixed. The middle column is the difference between the total and thermal density models, which is caused by nonthermal effects. The color scales change for each column according to the amplitude (A) labeled on the top.

with the minimum nonthermal heterogeneity that can still fit the data. Thus, it is possible that there are more nonthermal heterogeneity and, correspondingly, a different thermal regime that could still fit the data.

At 100- to 175-km depth, the cratonic keels dominate the chemical signature (Figure 6). In the transition zone (525- to 650-km depth, Figure 7), all the viscosity models show nonthermal or chemical anomalies

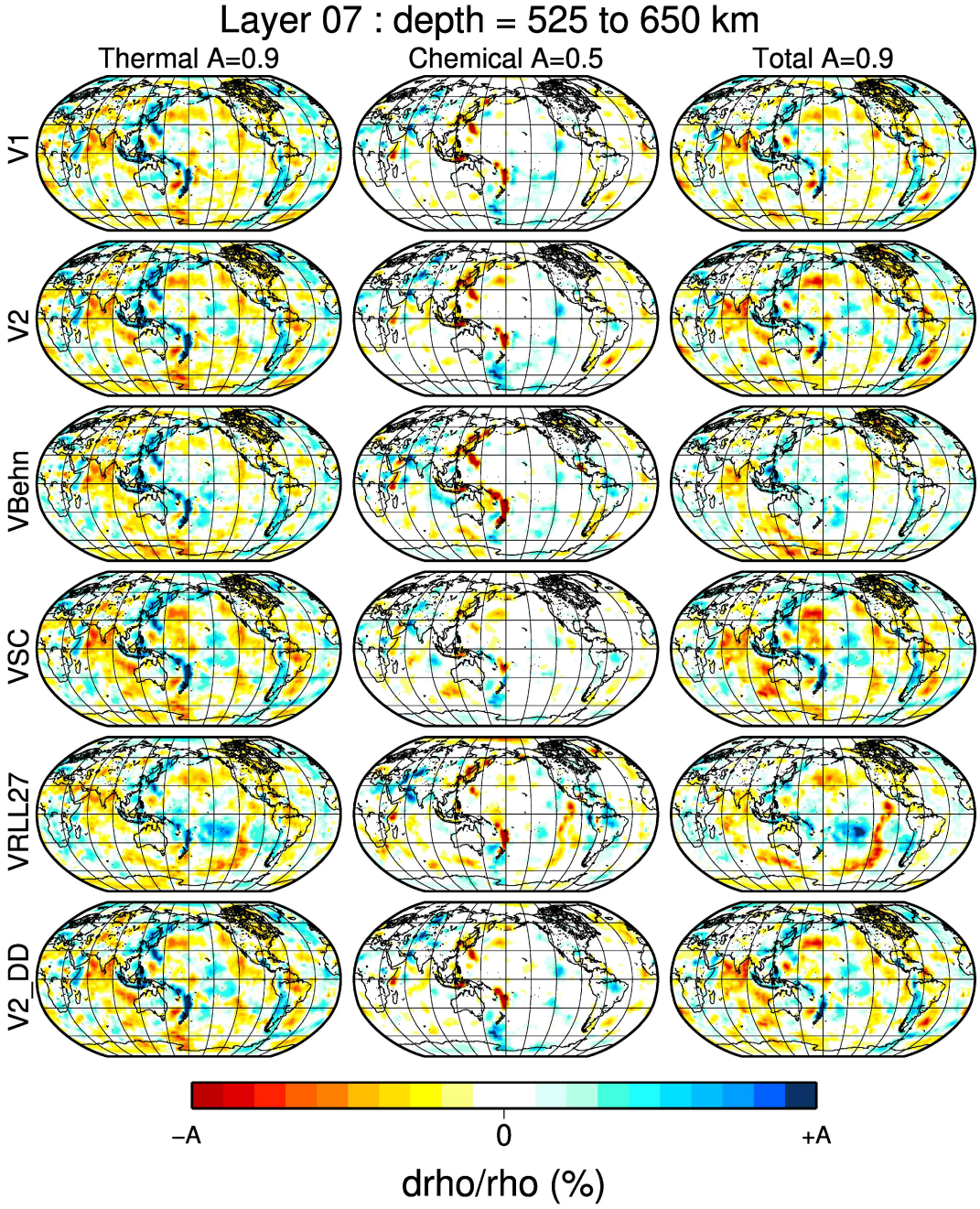

Figure 7. Lateral density variations derived from joint inversions between 525- and 650-km depth. The different columns are the same as in Figure 6. The nonthermal anomalies in the slabs of the western Pacific decrease the slab density predicted in the thermal density model.

in the slabs of the western Pacific that decrease the slab density. The signal is strongest for model VBehn and weakest for model VSC, but some buoyant nonthermal anomaly is seen in each model. Depression of the 660-km discontinuity in the subduction zone (Bina & Helffrich, 1994; Shearer & Masters, 1992) could explain this since we have not explicitly accounted for discontinuity topography in our inversions. The existence of metastable olivine inside slabs (Kawakatsu & Yoshioka, 2011; Lidaka & Suetsugu, 1992) could also decrease the density in deep slabs although that would also decrease the seismic velocity. In the midmantle (Figures 8 and 9), the nonthermal anomalies are short wavelength and relatively small. A common feature among all models is positive nonthermal density anomalies beneath southeast Africa

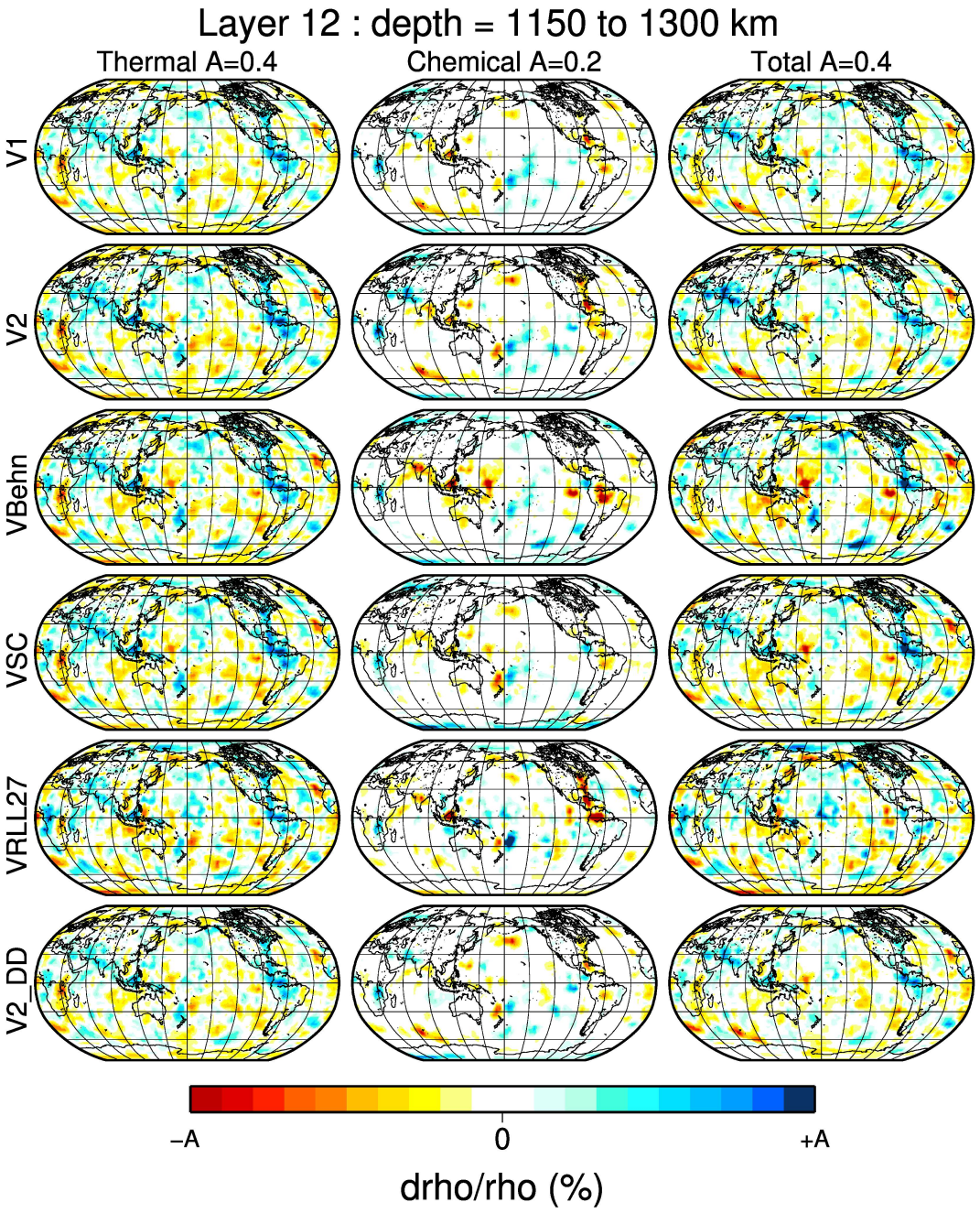

Figure 8. Lateral density variations derived from joint inversions between 1,150- and 1,300-km depth. The different columns are the same as in Figure 6. Two elongated positive density anomalies beneath southwestern Eurasia and North America can be seen in the thermal and total density models. Negative buoyant nonthermal anomalies are found beneath southeast Africa and the south-central Pacific.

and some regions in the south-central Pacific. These regions are strongly buoyant in the "thermal density" models but require an increase in density to fit the geodynamic data. In this depth range, many other non-thermal anomalies are seen, but they are not consistent among the models.

4.2. Characteristics of the LLSVPs

In the lowermost mantle, most of the models require positive nonthermal density anomalies in the center of the LLSVPs, though the amount required varies between different viscosity models (Figure 10). As a result,

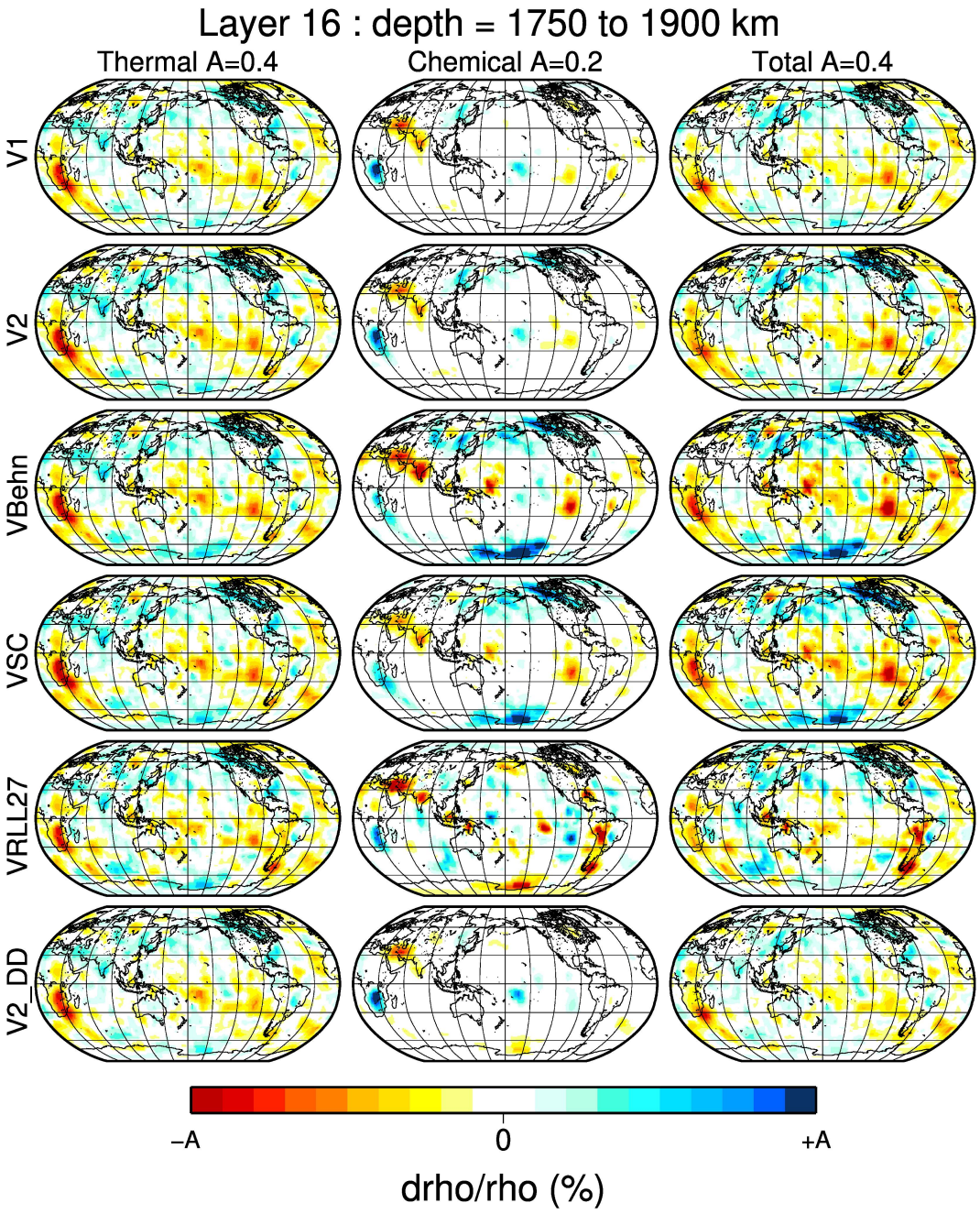

Figure 9. Lateral density variations derived from joint inversions between 1,750- and 1,900-km depth. The different columns are the same as in Figure 6. Buoyant nonthermal anomalies are seen beneath southwestern Eurasia but not North America.

the centers of the LLSVPs have overall neutral or negative buoyancy in the corresponding total density models. Using the V2 model, for example, about 21% of the area of the LLSVPs has neutral or negative buoyancy. The average derived scaling factor $\Delta R^{3D}_{\rho/V_S}$ in this central area is about −0.05 compared with 0.11 averaged over the whole of the LLSVPs. These values are similar for both the Pacific and African LLSVPs. The only exception is the VRLL27 model, which shows a limited amount of nonthermal density anomalies inside LLSVPs and predicts overall buoyant LLSVPs at the CMB. Surrounding the LLSVPs, however, there is buoyant mantle at the CMB, and for viscosity models V1, V2, and V2_DD, there is even negative nonthermal density (i.e., "superbuoyancy") beneath the EPR.

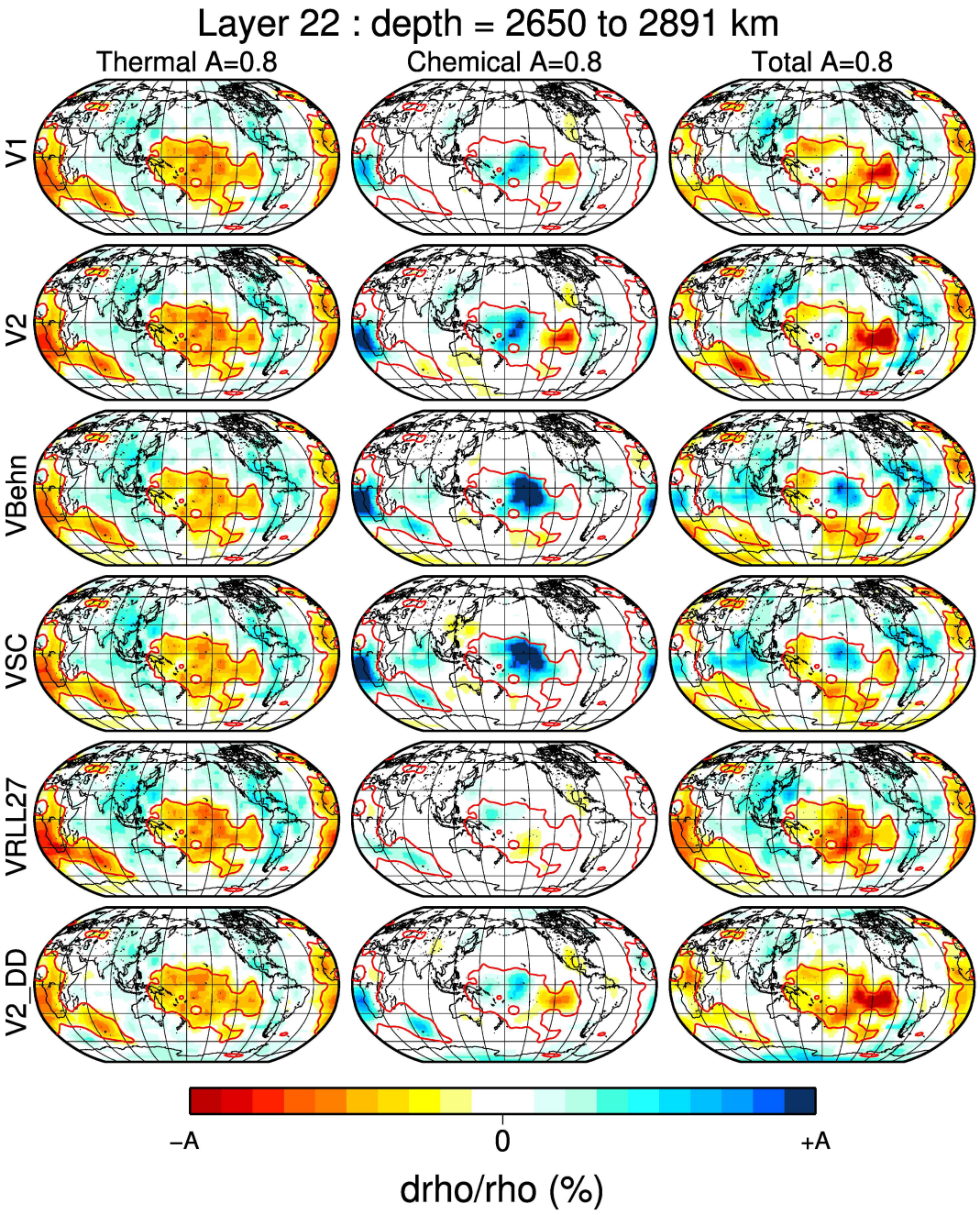

Figure 10. Lateral density variations derived from joint inversions at the deepest mantle. The different columns are the same as in Figure 6. Except for the model using VRLL27, all models require positive nonthermal density anomalies in the center of the LLSVPs. The center of the LLSVPs has overall neutral or negative buoyancy in the corresponding total density models. Red solid lines are the approximate edges of LLSVPs, which defined by 0.8% slow shear velocity in pure seismic tomography model TX2016 (Lu & Grand, 2016) at the CMB.

As opposed to chemical anomalies, the nonlinear effect of attenuation on the relation between temperature and shear velocity (Matas & Bukowinski, 2007) may be partly responsible for the inferred nonthermal anomalies. In hot (slow velocity) regions, temperature-dependent attenuation can increase the sensitivity of velocity to temperature and reduce the $R_{\rho/Vs}$. Therefore, the attenuation effect can partially explain the excess density needed in the LLSVP regions to satisfy the geodynamic data (see supporting information for details); however, this cannot explain the overall dense or neutral anomalies seen in the middle of the LLSVPs.

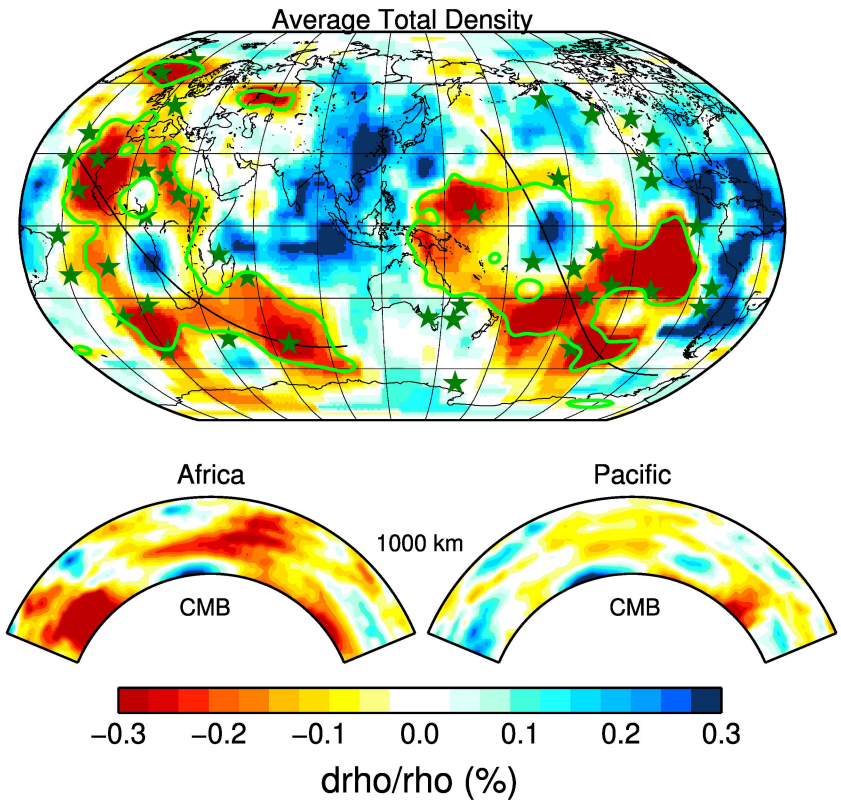

Figure 11. Average of V1, V2, VBehn, VSC, and V2_DD total density models at the CMB (2,650 to 2,891 km). Lateral average density variation in the deepest mantle (top). The scale is accentuated to illustrate buoyant versus dense regions. Black lines show the locations of the cross sections plotted in the bottom panel. Most hotspot locations (Steinberger, 2000) (green stars) are located over the buoyant parts of the LLSVPs. Two cross sections of average total density across the Pacific and Africa LLSVPs (bottom). The centers of the LLSVPs are overall denser than ambient mantle in the bottom 400 km, while material above and on the edges of the dense cores shows positive buoyancy. Green solid lines are the approximate edges of LLSVPs as described in Figure 10.

Given the short wavelength scatter in the inferred density models and the uncertainty in the actual viscosity, we averaged five total density models derived using different viscosities (V1, V2, VBehn, VSC, and V2_DD). The density model derived using VRLL27 is excluded here because of the large differences from the other four models as well as the poor data fit to the geodynamic data. In Figure 11, we show the deep mantle (2,650 to 2,891 km) density from our combined model as well as two cross sections through the African and Pacific LLSVPs, respectively. The centers of the LLSVPs are overall denser than ambient mantle in the bottom 400 km, while they are buoyant at the edges of LLSVPs as well as at shallower depths. We further note that these positive, nonthermal contributions to the total density anomalies extend upward from the LLSVP to midmantle depths (see middle column in Figure 9). The positive nonthermal density anomalies we found inside the LLSVPs could be explained by a potentially strong nonlinear effect of temperature-dependent attenuation or the existence of lateral chemical variation (e.g., iron enrichment or accumulated basaltic material from subduction) (Garnero et al., 2016). However, the overall negative or neutral buoyancy in the center of LLSVPs right above CMB rules out the option that the nonthermal density anomalies we found are due to attenuation alone. Given the radial resolving power of our long wavelength gravity and topography data, it is possible that the chemical density anomalies could be stronger but more focused at the CMB.

Our results indicate that the centers of the LLSVPs are chemically distinct from surrounding mantle, at least in the bottom 400 km of the mantle. The dense structure in the center of the LLSVPs (Figure 11) contradicts the joint inversion results found by Simmons et al. (2009) who found buoyant mantle throughout the LLSVPs. The difference is likely due to the increased *S* wave data coverage in the current inversion. Our

model is, however, similar to a later joint inversion model generated by Simmons et al. (2010), which included *P* wave data. Ishii and Tromp (1999) found dense anomalies at the base of the mantle beneath the LLSVPs with relatively more buoyant deep mantle in the circum-Pacific regions. Although our model has slightly dense mantle in the cores of the LLSVPs, the regions of very high D″ velocity around the circum-Pacific have the highest densities. This contradicts the results of Ishii and Tromp (1999), where a trade-off between mantle density and CMB topography likely had an influence on their results, whereas CMB topography and mantle density are self-consistent in our approach. However, in our models we have neglected the phase transition of perovskite to pPv. This phase transition is likely to be limited to the deepest layer in our model (D″) and perhaps is only relevant to the colder regions (e.g., Hirose, 2006). Given that the *S* velocity and density both increase in pPv, the circum-Pacific high-velocity regions may be explained by the phase transition accompanied by a higher temperature than our inversions imply. Further work is needed to unravel the complexities of the phase transition, chemistry, and temperature in the fast D″ regions.

Around the dense center of the LLSVPs, we find strongly buoyant material both above and on the edges of the dense cores (Figure 11). Figures 8 and 9 show some dense nonthermal density anomalies embedded within the overall buoyant material. Beneath South Africa, this signal is seen for all the viscosity models, while beneath the Pacific, there is more variation among models. The nonthermal density anomalies could be due to entrainment of the dense bottom material in upward flow but could also be due to nonlinear anelastic effects. On the other hand, due to the uncertainties in the mineral physics modeling results, we performed grid searches to find the best fit scaling factors assuming that seismic variations are thermal. Therefore, the nonthermal density anomalies found in our joint inversion are likely a minimum amount required by the geodynamic data. It is possible that thermal and nonthermal effects compensate each other and are muted in our nonthermal inversions to some extent, though exact compensation is unlikely since the sensitivities of elastic modulus and density to thermal and chemical effect are usually quite different. If this type of compensation exists in the LLSVPs, it means that there is even more chemical heterogeneity than we found.

4.3. Robustness and Limitations of the Joint Inversion

In order to better understand the relationship between our derived density models and each geodynamic constraint used in the inversion, we followed the same procedures to perform both thermal and nonthermal joint inversions with individual geodynamic constraints removed. The results are plotted in Figure S8. Among these models, the distribution of density anomalies generally agrees with each other, which indicates the internal consistency among the geodynamic constraints we used. However, the amplitudes of density anomalies vary in these models, which show the different sensitivity of density distribution to different geodynamic constraints. The gravity field, in particular, places the strongest constraints on the deepest mantle.

It is useful at this point to consider the impact of smoothing on our density heterogeneity inferences. We recall that the smoothing weight λ_D and geodynamic data weight λ_G are based on an L-curve analysis (Figure 4). The trade-off curve method is a conventional way to determine smoothing or data weight in an inversion, with some degree of subjectivity in the final weight selected. We also adjusted the regularization such that the nonthermal and thermal models have the same roughness. This was rather arbitrary, so in Figure S9, we show joint inversion results using different smoothing weights in nonthermal inversions for the V2 model. The choice of smoothing weight does not significantly affect the large-scale features described above. In Figure S10, joint inversion results using different geodynamic data weights (λ_G) for the V2 model are shown. When λ_G is small, the dense center of the LLSVPs in the total density field is not seen even though there are still positive nonthermal density anomalies there. This is because when λ_G is small, the inversion is dominated by seismic data alone, which tends to overpredict the buoyancy of the LLSVPs. Due to the smoothing regularization in the nonthermal inversion, the inversion failed to find enough nonthermal density in the center of the LLSVPs to recover the total density field. This comparison, in fact, further illustrates the importance of jointly inverting the seismic and geodynamic data.

The geodynamic importance of nonthermal or compositional heterogeneity in the mantle, which is quantified in Table 1, is explicitly illustrated in Figure S11, which presents maps of each of the geodynamic observables and the corresponding predictions obtained with both purely thermal and total models of density heterogeneity, where the latter incorporates the nonthermal density contributions. The spatial match between the predicted and observed dynamic surface topography is very good and closely parallels the excellent fit to the free-air gravity anomalies, which are both quantified in Table 1. The overall amplitude of

predicted CMB topography (Figure S11) with both models is within the bounds of recent studies (e.g., Deschamps & Li, 2019; Garcia & Souriau, 2000). The impact of nonthermal (compositional) heterogeneity is still most strongly manifested in the prediction of CMB topography, which clearly shows the "footprint" of intrinsically dense heterogeneity embedded within the LLSVP, under the central Pacific Ocean and under southern Africa. Long wavelength-predicted dynamic surface and CMB topography are also shown in Figure S12.

It has been proposed that volcanic hotspots are preferentially located above the margins of the two LLSVPs found in seismic tomography (e.g., Steinberger & Torsvik, 2012; Thorne et al., 2004) although there are studies that show that the correlation might not be statistically reliable (Austermann et al., 2014; Davies et al., 2015). We plot hotspot locations (Steinberger, 2000) on top of our summary density model at the CMB (Figure 11). About 60% of hotspots are located over the buoyant parts of the LLSVPs. Several hotspots located along the western and southern margin of North America are far away from LLSVPs and may have different origins (e.g., thermal instabilities triggered by descent of ancient subducted material). If they are excluded from the calculation, the percentage increases to ~68%. Even for hotspots located over dense parts of the LLSVPs, none of them are located in the center of the dense cores. Our results indicate that LLSVPs have a chemically dense core that is surrounded by hot mantle that is associated with upwelling plumes resulting in "hotspots" in some cases. French and Romanowicz (2015) found that low-velocity regions inside LLSVPs might concentrate around the feet of major hotspots. However, our predicted mantle upwellings above the CMB are more continuous instead of isolated structures as inferred in the French and Romanowicz (2015) model.

Viscosity model VRLL27 yielded the poorest data fits. It was derived using only very long wavelength geoid anomalies as a constraint (as in Forte & Peltier, 1987, who also showed that a viscosity increase near 1,200-km depth was compatible with long wavelength geoid data) and does not resolve major viscosity variations in the upper mantle corresponding to the lithosphere and asthenosphere that are evident in the other viscosity models, which employ more geodynamic constraints. It is therefore not surprising that model VRLL27 did not provide a better fit to the full suite of geodynamic constraints. We included this viscosity model in our study as an important test case to illustrate the impact of using a drastically different viscosity model in the joint inversions. The poor fit to geodynamic data using this model is therefore encouraging, to the extent that it demonstrates the sensitivity to assumed viscosity in the joint inversions.

The variability in current inferences of the depth dependence of mantle viscosity (Figure 1) reflects a long-standing difficulty in obtaining robust resolution of the spatial variability of the rheological properties of the mantle. The difficulty in uniquely resolving radial viscosity variations is a facet of the much larger challenge concerning the determination of lateral viscosity variations (LVV) throughout the mantle that reflect realistic constraints on the microphysical creep properties of mantle rocks, while also yielding a satisfactory fit to the full suite of convection-related surface observables that are employed in the joint tomography inversions presented above.

Recent efforts by Yang and Gurnis (2016) to reconcile both gravity anomalies and topography in mantle flow calculations suggest quite modest LVV in the sublithospheric mantle indicating that several opposing microphysical controls on rheology may be important, as found by Glišović et al. (2015). The Yang and Gurnis (2016) study extends earlier work by Ghosh et al. (2010) and Forte, Moucha, et al. (2010) showing similarly modest impacts of LVV. Indeed, as shown in Moucha et al. (2007), the impact of LVV is overshadowed by much stronger variability in the geodynamic predictions associated with uncertainties in the tomography models themselves. To underline these points, Figure S13 shows the impact of LVV throughout the mantle (as calculated by Glišović et al., 2015) on dynamic surface topography calculated by Kajan et al. (2018). The effect of these LVV is modest and much smaller than the differences between topography predictions obtained using two distinct tomography models, where each model was optimized to yield a best fit to the geodynamic surface observables.

5. Mantle Flow Simulations

5.1. Present-Day Mantle Flow Fields

Using the total density models derived in the joint inversions, as well as their corresponding radial viscosity profiles, we can determine the present-day mantle flow fields for each model (Behn et al., 2004; Forte, Quéré,

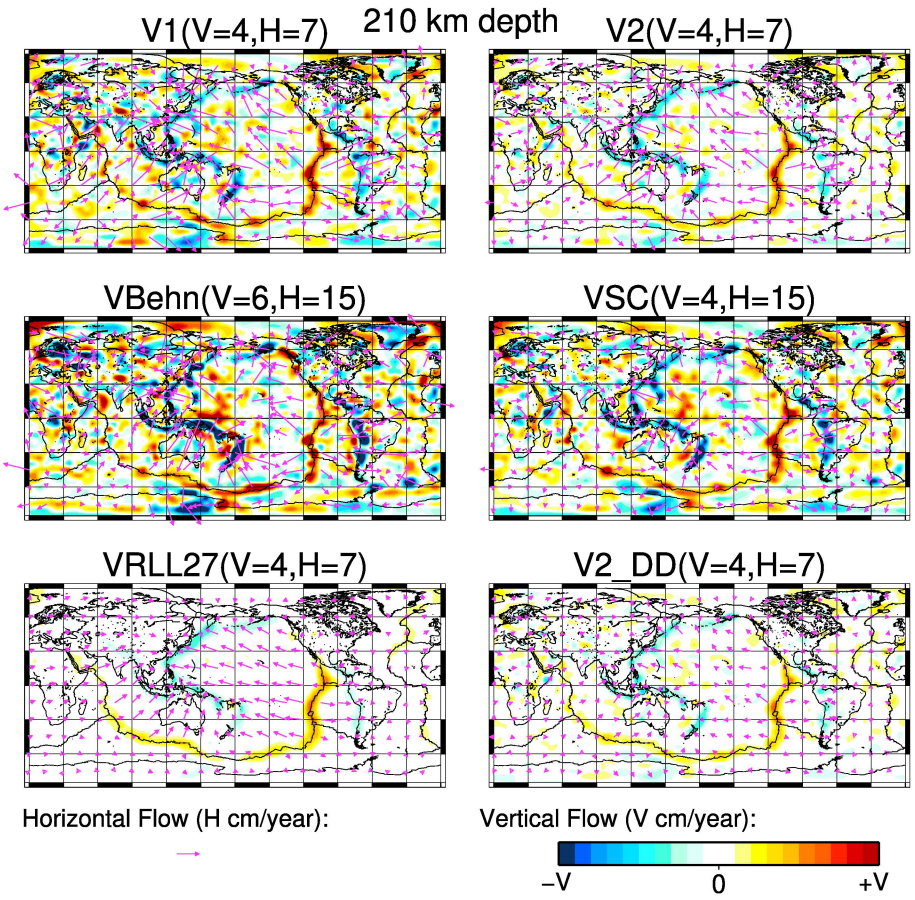

Figure 12. Predicted present-day convective flow using the density models derived from the joint inversions at 210-km depth. The background color shows the direction and amplitude of vertical flow; blue represents downwelling flow, and red represents upwelling flow. Purple arrows show the orientation and amplitude of horizontal flow. Note that the scales for vertical and horizontal flows are different in each plot and are labeled on the top.

et al., 2010; Mitrovica & Forte, 2004; Rudolph et al., 2015; Steinberger & Calderwood, 2006). The vertical and horizontal flows at selected depths are plotted in Figures 12 to 14. The most striking difference in flow predicted by the different viscosity models is the magnitude of the flow velocities. Viscosity models VBehn and VSC yield predictions with substantially higher horizontal mantle flow velocities in the shallow upper mantle (Figure 12) than those by viscosity models V1, V2, V2_DD, and VRLL27. This difference is mainly due to the substantially reduced absolute values of viscosity in the asthenosphere in the VBehn and VSC models, which were rescaled to match the present-day surface plate velocities (see section 2.2).

Other than the magnitude of flow velocities, the different viscosity-density models produce patterns of upper-mantle flow with many similarities although there are also interesting differences. At 220-km depth (Figure 12), the vertical and horizontal flow patterns for the models are similar in most regions with the exception of the flow derived from the VRLL27 viscosity model. The correlation coefficients between vertical flow for the V1 model and the V2, VBehn, VSC, and VRLL27, V2_DD models are 0.95, 0.76, 0.90, 0.65, and 0.94, respectively (Table 2). In terms of the horizontal flow direction, for each viscosity model (excluding VRLL27), at least 53% of points on a 5 by 5 grid have horizontal flow directions within 30° of those in model V1, while at least 77% are within 60° (Table 2). We find good correlations between predicted shallow mantle flow fields and surface tectonic environments. Downwellings are predicted under subduction regions, and upwellings are found beneath mid-ocean ridges, as expected. Apart from the VRLL27 model, we also find individual-focused upwellings beneath many hotspot locations (Steinberger, 2000), including the Cape Verde, Hoggar, Cameroon, and Darfur hotspots in Africa, the Bowie and Cobb hotspots in the northeast Pacific, and most of the hotspots in the Pacific, Atlantic, and southern Indian Ocean (Figure S14). In contrast to flow models (Forte et al., 2015; Forte, Quéré, et al., 2010; Rowley et al., 2016) derived using previous joint

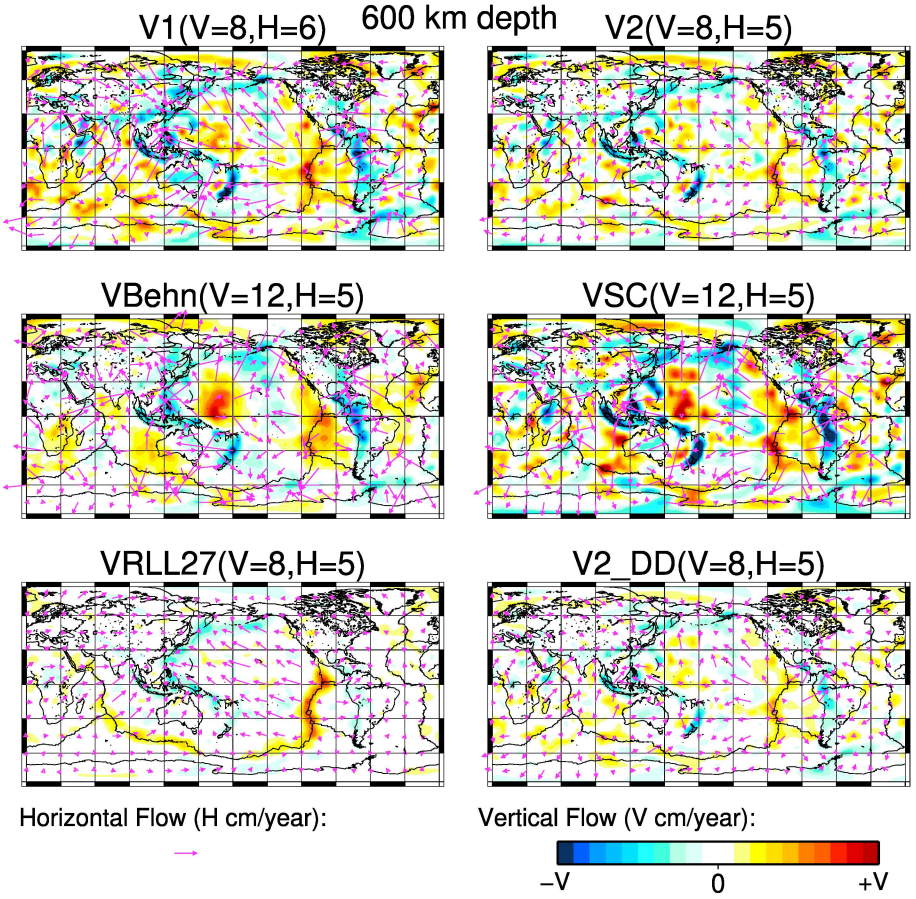

Figure 13. Predicted present-day convective flow using the density models derived from the joint inversions at 600-km depth. The colors and arrows have the same meaning as in Figure 12.

tomography inversions (Simmons et al., 2007, 2009, 2010), our new flow models yield strongly focused upwellings beneath the Caroline and East Australia hotspots, though the horizontal flows around these regions are different among models (Figure 12). The good correlation with surface tectonic features using a variety of independent viscosity models provides encouraging support for the reliability of the predicted flow fields.

A noteworthy difference in shallow mantle flow predicted by the different viscosity models concerns the Caroline hotspot in the western Pacific. Although all models have upwelling beneath the hotspot, the VBehn and VSC viscosity models (which are characterized by lower viscosity in the asthenosphere) predict stronger upward flow there than the other models. This creates a radial pattern of flow away from the hotspot for models VBehn and VSC, whereas the other models produce asthenospheric flow basically parallel to the plate motion. This difference will produce different strains at shallow mantle depths and thus predict different seismic anisotropy (e.g., Becker et al., 2003; Conrad et al., 2007; Forte, Quéré, et al., 2010; Gaboret et al., 2003). Thus, seismic anisotropy measurements could provide useful additional constraints for discriminating among the different viscosity models.

At 600-km depth (Figure 13), the vertical flow patterns are again similar but show more differences than at shallower depths (Table 2). Interestingly, the most notable common feature in all six models is strong upwelling beneath the EPR, particularly in the central part. Upwelling beneath the Caroline hotspot is stronger than at 210 km; this is especially true for the VBehn and VSC models. Other large-scale upwellings exist beneath Iceland, Cape Verde, southern Africa, and the southern Indian Ocean but are more variable among models. The horizontal flow fields at this depth are also more variable among models than at shallower depths (Table 2). Strong radial flow away from the Caroline hotspot is again predicted by models VBehn and VSC but not by the other models.

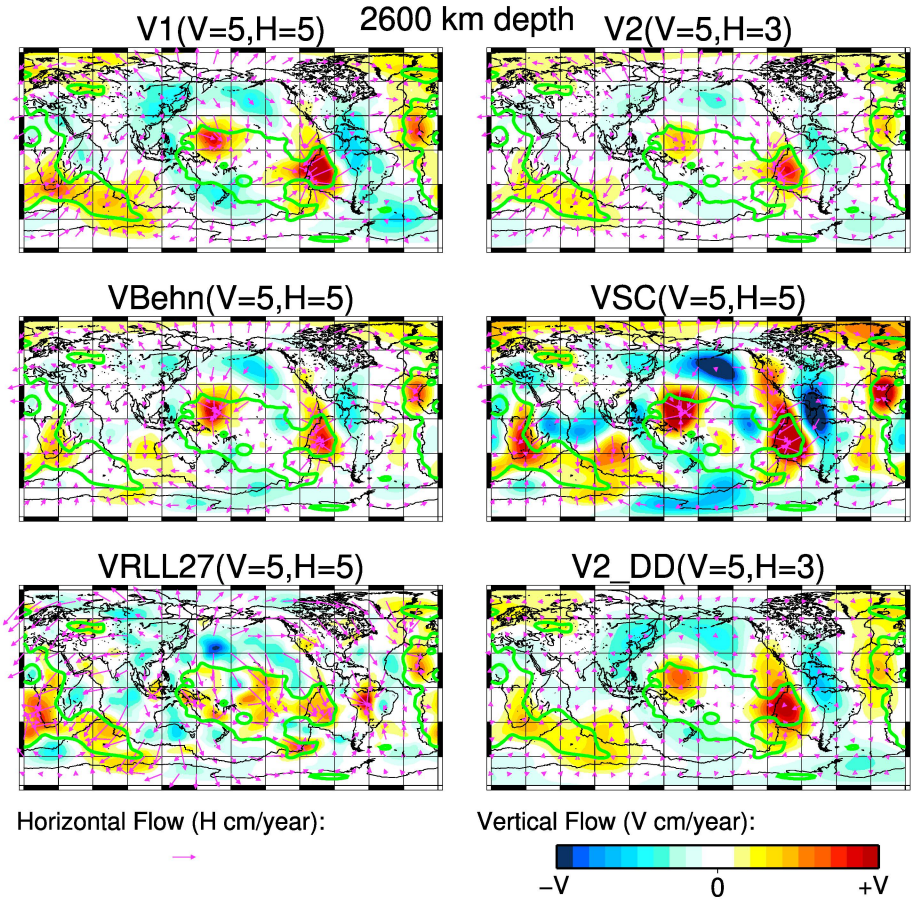

Figure 14. Predicted present-day convective flow using the density models derived from joint inversions at 2,600-km depth. The colors and arrows have the same meaning as in Figure 12. Green solid lines are the approximate edges of LLSVPs as described in Figure 10.

In the deep lower mantle, the similarities between models increase again and are comparable to those at 210-km depth, with the exception of the VRLL27 model (Table 2; Figure 14). For the five models that are similar, four isolated large-scale upwellings occur beneath the EPR, the Caroline hotspot region, the Cape Verde island region, and the southern Africa/India Ocean region, respectively. Because of the dense LLSVP cores, the models do not predict deep upwelling directly above the center of LLSVPs. All deep mantle upwellings are surrounded by downwellings, with mantle material swept toward them. We note that the above observations also hold true for our model with strongly reduced viscosity in D″ (V2_DD). In our inversions, these large-scale upwellings are the dominant dynamic structures in the deep mantle.

Conrad and Behn (2010) used a simple constant-value scaling of seismic velocity to density using seismic model S20RTS (Ritsema et al., 2004) to simulate mantle convection using the VBehn viscosity model. They found a large deep mantle upwelling beneath the mid-Pacific above the Pacific LLSVP that resulted in eastward asthenospheric flow toward the EPR. Their model along a cross section through the Pacific is shown in Figure 15h and is labeled as VCB. Using a density model derived by joint inversion (Simmons et al., 2009), Rowley et al. (2016) computed a mantle flow model that showed a deep-seated mantle upwelling beneath the EPR with sublithospheric flow away from the ridge. They postulate that this large deep mantle upwelling is a major contributor to the driving force producing Pacific plate motion and is also the cause of the longitudinal fixity of the central EPR. The viscosity model used by Rowley et al. (2016) was model V2. In Figures 15b–15g, we show cross sections through the six flow models, which are compared to model VCB. All six models yield a strong mantle-wide upwelling under the EPR with asthenospheric flow away from the ridge, similar to the Rowley et al. (2016) results. We conclude that the difference in flow predictions between the two studies is due to the modeling of mantle density anomalies and not to the different

Table 2
Similarity Between Derived Flow Fields Using Different Viscosity Models[a]

Depth (km)	Model	Vertical flow CC	Angular difference of horizontal flow ($\Delta\theta$)		
			$\Delta\theta < 30°$	$30° < \Delta\theta < 60°$	$\Delta\theta > 60°$
210	V1	1	100%	0%	0%
	V2	0.95	83.2%	10.9%	5.9%
	VBehn	0.76	53.3%	23.9%	22.8%
	VSC	0.90	63.1%	21.0%	15.9%
	VRLL27	0.65	47.5%	25.6%	26.9%
	V2_DD	0.94	84.6%	8.9%	6.5%
600	V1	1	100%	0%	0%
	V2	0.95	73.1%	17.8%	9.1%
	VBehn	0.74	41.1%	24.4%	34.5%
	VSC	0.86	52.6%	24.8%	22.6%
	VRLL27	0.54	38.2%	29.2%	32.6%
	V2_DD	0.95	76.0%	16.6%	7.3%
2,600	V1	1	100%	0%	0%
	V2	0.95	93.5%	5.2%	1.3%
	VBehn	0.83	60.8%	23.7%	15.5%
	VSC	0.79	61.6%	22.0%	16.4%
	VRLL27	0.46	37.1%	27.4%	35.5%
	V2_DD	0.93	82.9%	14.0%	3.1%

[a]All the calculations used V1 as the reference model and derived based on 5° × 5° grid. The angular difference of horizontal flow's direction at each grid point is used in the calculation.
Abbreviation: CC = correlation coefficients.

viscosity models. Seismic model S20RTS (Ritsema et al., 1999) is similar to the pure seismic model we derived, implying that the differences in the 3D density anomalies used in our study and by Conrad and Behn (2010) are mainly due to the manner in which the latter study converted seismic heterogeneity into density anomalies.

5.2. Potential Impact of LVV

Forte, Moucha, et al. (2010) showed that the locations and relative amplitudes of the long-wavelength to intermediate-wavelength vertical convective motions (i.e., for harmonic degrees ≤32) should be robustly mapped out using only a radial varying viscosity. In that regard, we underline that the calculations of viscous flow kernels employed in the joint inversions incorporate mobile tectonic plates as a surface boundary condition and these plates, characterized by rigid interiors and weak boundaries, are arguably the strongest expression of LVV in the mantle. The dynamical feedback from such manifestations of laterally heterogeneous, plate-like mechanics at the top of the mantle is a key ingredient in all our predictions of geodynamic observables (Figure S11) and of mantle flow (Figures 12–15). Therefore, our derived flow models should be reliable in terms of vertical flow and somewhat reliable in terms of horizontal flow, especially in those sublithospheric regions where the gradients of LVV are small. We further explore and illustrate this robustness in Figure S15, which shows the extent to which vertical and horizontal flow predictions, as calculated by Kajan et al. (2018), are modified by LVV, where the latter are calculated from combined geodynamic and mineral physical constraints on mantle viscosity by Glišović et al. (2015). It is evident that even in regions with substantial horizontal viscosity contrasts, as in the shallow upper mantle, the pattern of vertical and horizontal flow is very similar to that predicted using a simple 1D viscosity model, even though the local magnitudes of vertical/horizontal flow are modified by the LVV.

We therefore suggest that, until such time when joint inversions can be carried out that fully incorporate realistic mineral physical predictions of LVV, the potential impact of such LVV on predicted mantle dynamics remains an open issue requiring further work. In this regard, an effort is currently underway to numerically calculate viscous-flow Green functions (e.g., as in Forte & Peltier, 1987) that incorporate arbitrary 3D viscosity heterogeneity throughout the mantle, with the objective of using such Green functions in a new generation of joint tomography inversions. The results of this numerically intensive work will be documented in future reports. Determining mantle flow thus remains a challenging problem, but robust assessments of mantle flow models should take into account observable geodynamic constraints that complement

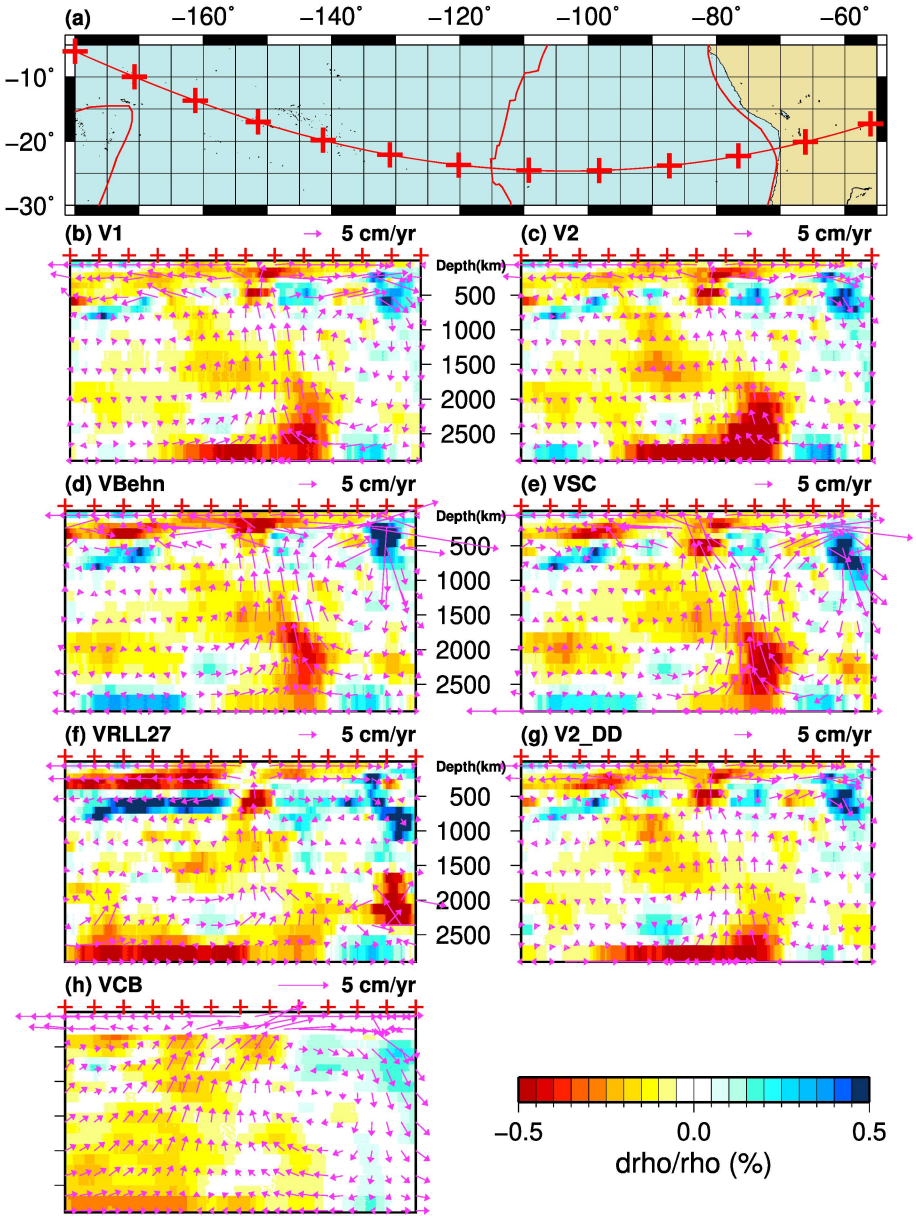

Figure 15. (a) Cross sections across the East Pacific Rise showing mantle density anomalies as a function of depth together with computed flow velocities. (b–g) Background color shows density anomalies derived from the joint inversions using different viscosity models. Purple arrows are the orientation and amplitude of the predicted flow field projected onto the great circle plane. (h) Predicted flow field by Conrad and Behn (2010) for viscosity "VBehn" on top of the density model scaled from the seismic model S20RTS (Ritsema et al., 1999).

global seismic data employed in traditional tomography inversions. The geodynamic data are key, because they provide direct constraints on the integrated mantle buoyancy (and mantle rheology) that drives the present-day mantle convective flow.

6. Conclusions

We performed joint inversions of seismic and geodynamic data using six different viscosity models. We first attempted to fit the data using an optimized scaling between seismic velocity and density assuming that mantle heterogeneity is due to thermal variations. The resulting density model was then modified to better fit the geodynamic data. Although this approach initially makes an assumption about the cause of

heterogeneity, there is no doubt that large lateral temperatures do exist in the mantle and, thus, substantially contribute to the density field. We therefore feel that this is a conservative approach that may underestimate chemical heterogeneity in the mantle but should nonetheless yield models of the total density anomalies that are properly constrained by fundamental geodynamic observables. We found, for all the viscosity profiles we tested, that we could not explain the data assuming that heterogeneity is due to thermal affects alone. Nonthermal origin density anomalies are required in all the inversion tests to explain the geodynamic data, though the amplitudes of the required nonthermal heterogeneity vary between models. Notwithstanding these variable inferences of nonthermal heterogeneity magnitudes, all the models require strong nonthermal anomalies near the top of the mantle (in the cratonic lithosphere) and at the bottom of the mantle (in the LLSVPs). Specifically, we found that the cores of the LLSVPs near the CMB are either neutrally buoyant or dense. In contrast, the edges of the LLSVPs are buoyant. We also find that the highest density regions at the base of the mantle are in regions of high seismic velocity.

The flow fields we obtained using different viscosity models show many common large-scale features, particularly in the lower mantle. As discussed above, an uncertainty in our modeling is due to the lack of incorporation of LVV in the sublithospheric mantle. To address this uncertainty, we explored the impact of a recent model of LVV (Glišović et al., 2015) on mantle flow predictions, shown in Figures S13 and S15, and we found that the impact of such LVV on predicted surface observables is estimated to be less than the current uncertainties in global tomography models. These results show how LVV may focus some of the flow patterns we computed with radial viscosity variations, but given the similarity in the flow patterns predicted with different 1D viscosity models, it is unlikely that the large-scale flow would be significantly different using a more complex 3D rheology. These findings suggest that future work is needed that incorporates a realistic mineral-physical representation of rheology in the predicted flow modeling, while also ensuring that convection-related observables are adequately fit. The latter condition is a key requirement, as shown by the results we presented above.

Although there are large-scale similarities among the flow models we developed, there are significant differences in specific places in the upper mantle. The differences are likely to produce different orientations of anisotropy, but a full strain analysis would be required to predict such anisotropy. This is beyond the scope of this work but is a promising direction for future work (e.g., Becker et al., 2003; Conrad et al., 2007; Gaboret et al., 2003). It is significant, however, that the large-scale flows we derived do differ significantly from a flow model derived by directly scaling a seismic model to density. Considering previous studies that have employed such a constant velocity-density scaling (e.g., Liu et al., 2008; Spasojevic et al., 2009; Steinberger, 2016), this finding underlines that, even though the magnitude of chemical heterogeneity inferred in the joint inversions is conservative, the resulting flow predictions will differ significantly from these previous tomography-based studies.

Acknowledgments
We thank Incorporated Research Institutions for Seismology, Data Management Center (IRIS DMC, https://ds.iris.edu/ds/nodes/dmc/), Observations & Research Facilities for European Seismology (ORFEUS, https://www.orfeus-eu.org/), Northern California Earthquake Data Center (NECDC, http://ncedc.org/), F-net Broadband Seismograph Network (F-net, http://www.fnet.bosai.go.jp/), and Canadian National Seismic Network (CNSN, http://www.earthquakescanada.nrcan.gc.ca/stndon/CNDC/) for providing data used in this study. We also thank Jung-Fu Lin, Thorsten Becker, Suyu Fu, Petar Glišović, and Paul Bremner for valuable discussions. This research was supported by NSF Grant EAR-1648770 as well as by the Jackson School of Geosciences at the University of Texas at Austin. A. M. F. acknowledges support of this work provided by NSF Grant EAR-1903108 as well as by the University of Florida. E. J. G. acknowledges support provided by NSF Grant EAR-1648817.

References

Amante, C., & Eakins, B. W. (2009). ETOPO1 1 arc-minute global relief model: Procedures, data sources and analysis. In *NOAA Technical Memorandum NESDIS NGDC-24*. Boulder, CO: National Geophysical Data Center, NOAA. https://doi.org/10.7289/V5C8276M

Anderson, D. L., & Hart, R. S. (1978). Attenuation models of the Earth. *Physics of the Earth and Planetary Interiors*, *16*(4), 289–306. https://doi.org/10.1016/0031-9201(78)90068-7

Anderson, O. L., & Isaak, D. G. (1995). Elastic constants of mantle minerals at high temperature. In T. J. Ahrens (Ed.), *Mineral physics & crystallography: A handbook of physical constants*, (Vol. 2, pp. 64–97). Washington, DC: American Geophysical Union.

Argus, D. F., Gordon, R. G., Heflin, M. B., Ma, C., Eanes, R. J., Willis, P., et al. (2010). The angular velocities of the plates and the velocity of Earth's centre from space geodesy. *Geophysical Journal International*, *180*(3), 913–960. https://doi.org/10.1111/j.1365-246X.2009.04463.x

Austermann, J., Kaye, B. T., Mitrovica, J. X., & Huybers, P. (2014). A statistical analysis of the correlation between large igneous provinces and lower mantle seismic structure. *Geophysical Journal International*, *197*(1), 1–9. https://doi.org/10.1093/gji/ggt500

Bassin, C., Laske, G., & Masters, G. (2000). The current limits of resolution for surface wave tomography in North America. *Eos, Transactions Amercian Geophysical Union*, *81*, F897.

Becker, T. W., Kellogg, J. B., Ekström, G., & O'Connell, R. J. (2003). Comparison of azimuthal seismic anisotropy from surface waves and finite strain from global mantle-circulation models. *Geophysical Journal International*, *155*(2), 696–714. https://doi.org/10.1046/j.1365-246X.2003.02085.x

Behn, M. D., Conrad, C. P., & Silver, P. G. (2004). Detection of upper mantle flow associated with the African superplume. *Earth and Planetary Science Letters*, *224*(3–4), 259–274.

Bina, C. R., & Helffrich, G. (1994). Phase transition Clapeyron slopes and transition zone seismic discontinuity topography. *Journal of Geophysical Research: Solid Earth*, *99*(B8), 15,853–15,860. https://doi.org/10.1029/94JB00462

Birch, F. (1978). Finite strain isotherm and velocities for single-crystal and polycrystalline NaCl at high pressures and 300°K. *Journal of Geophysical Research: Solid Earth (1978–2012)*, *83*(B3), 1257–1268. https://doi.org/10.1029/JB083iB03p01257

Bunge, H.-P., Hagelberg, C., & Travis, B. (2003). Mantle circulation models with variational data assimilation: Inferring past mantle flow and structure from plate motion histories and seismic tomography. *Geophysical Journal International*, *152*(2), 280–301.

Burke, K., Steinberger, B., Torsvik, T. H., & Smethurst, M. A. (2008). Plume generation zones at the margins of large low shear velocity provinces on the core-mantle boundary. *Earth and Planetary Science Letters*, *265*(1), 49–60. https://doi.org/10.1016/j.epsl.2007.09.042

Cammarano, F., Goes, S., Vacher, P., & Giardini, D. (2003). Inferring upper-mantle temperatures from seismic velocities. *Physics of the Earth and Planetary Interiors*, *138*(3), 197–222. https://doi.org/10.1016/S0031-9201(03)00156-0

Conrad, C. P., & Behn, M. D. (2010). Constraints on lithosphere net rotation and asthenospheric viscosity from global mantleflow models and seismic anisotropy. *Geochemistry, Geophysics, Geosystems*, *11*, Q05W05. https://doi.org/10.1029/2009GC002970

Conrad, C. P., Behn, M. D., & Silver, P. G. (2007). Global mantle flow and the development of seismic anisotropy: Differences between the oceanic and continental upper mantle. *Journal of Geophysical Research: Solid Earth*, *112*(B07317), B07317. https://doi.org/10.1029/2006JB004608

Davies, D. R., Goes, S., Davies, J., Schuberth, B., Bunge, H.-P., & Ritsema, J. (2012). Reconciling dynamic and seismic models of Earth's lower mantle: The dominant role of thermal heterogeneity. *Earth and Planetary Science Letters*, *353*, 253–269.

Davies, D. R., Goes, S., & Sambridge, M. (2015). On the relationship between volcanic hotspot locations, the reconstructed eruption sites of large igneous provinces and deep mantle seismic structure. *Earth and Planetary Science Letters*, *411*, 121–130. https://doi.org/10.1016/j.epsl.2014.11.052

Dehant, V., Laguerre, R., Rekier, J., Rivoldini, A., Triana, S. A., Trinh, A., et al. (2017). Understanding the effects of the core on the nutation of the Earth. *Geodesy and Geodynamics*, *8*(6), 389–395.

Deschamps, F., Kaminski, E., & Tackley, P. J. (2011). A deep mantle origin for the primitive signature of ocean island basalt. *Nature Geoscience*, *4*(12), 879–882.

Deschamps, F., & Li, Y. (2019). Core-mantle boundary dynamic topography: Influence of postperovskite viscosity. *Journal of Geophysical Research: Solid Earth*, *124*, 9247–9264. https://doi.org/10.1029/2019JB017859

Ding, H., & Chao, B. F. (2018). A 6-year westward rotary motion in the Earth: Detection and possible MICG coupling mechanism. *Earth and Planetary Science Letters*, *495*, 50–55.

Duffy, T. S., & Anderson, D. L. (1989). Seismic velocities in mantle minerals and the mineralogy of the upper mantle. *Journal of Geophysical Research: Solid Earth*, *94*(B2), 1895–1912. https://doi.org/10.1029/JB094iB02p01895

Durek, J. J., & Ekström, G. (1996). A radial model of anelasticity consistent with long-period surface-wave attenuation. *Bulletin of the Seismological Society of America*, *86*(1A), 144–158.

Dziewonski, A. M., & Anderson, D. L. (1981). Preliminary reference Earth model. *Physics of the Earth and Planetary Interiors*, *25*(4), 297–356. https://doi.org/10.1016/0031-9201(81)90046-7

Fei, Y. (1995). Thermal expansion. In T. J. Ahrens (Ed.), *Mineral physics & crystallography: A handbook of physical constants*, (Vol. 2, pp. 29–44). Washington, DC: American Geophysical Union.

Finger, L. W., & Ohashi, Y. (1976). The thermal expansion of diopside to 800 degrees and a refinement of the crystal structure at 700 degrees. *American Mineralogist*, *61*(3–4), 303–310.

Fiquet, G., Dewaele, A., Andrault, D., Kunz, M., & Le Bihan, T. (2000). Thermoelastic properties and crystal structure of $MgSiO_3$ perovskite at lower mantle pressure and temperature conditions. *Geophysical Research Letters*, *27*(1), 21–24. https://doi.org/10.1029/1999GL008397

Flesch, L. M., Li, B., & Liebermann, R. C. (1998). Sound velocities of polycrystalline $MgSiO_3$-orthopyroxene to 10 GPa at room temperature. *American Mineralogist*, *83*(5–6), 444–450. https://doi.org/10.2138/am-1998-5-604

Forte, A., Peltier, W., Dziewonski, A., & Woodward, R. (1993). Dynamic surface topography: A new interpretation based upon mantle flow models derived from seismic tomography. *Geophysical Research Letters*, *20*(3), 225–228. https://doi.org/10.1029/93GL00249

Forte, A. M. (2007). Constraints on seismic models from other disciplines—Implications for mantle dynamics and composition. In G. Schubert (Ed.), *Treatise of geophysics*, (Vol. 1, pp. 805–858). Amsterdam, Netherlands: Elsevier Science.

Forte, A. M., & Mitrovica, J. X. (2001). Deep-mantle high-viscosity flow and thermochemical structure inferred from seismic and geodynamic data. *Nature*, *410*(6832), 1049–1056. https://doi.org/10.1038/35074000

Forte, A. M., Moucha, R., Simmons, N. A., Grand, S. P., & Mitrovica, J. X. (2010). Deep-mantle contributions to the surface dynamics of the North American continent. *Tectonophysics*, *481*(1–4), 3–15.

Forte, A. M., & Peltier, R. (1991). Viscous flow models of global geophysical observables: 1. Forward problems. *Journal of Geophysical Research: Solid Earth*, *96*(B12), 20,131–20,159. https://doi.org/10.1029/91JB01709

Forte, A. M., & Peltier, W. R. (1987). Plate tectonics and aspherical Earth structure: The importance of poloidal-toroidal coupling. *Journal of Geophysical Research: Solid Earth*, *92*(B5), 3645–3679. https://doi.org/10.1029/JB092iB05p03645

Forte, A. M., & Peltier, W. R. (1994). The kinematics and dynamics of poloidal-toroidal coupling in mantle flow: The importance of surface plates and lateral viscosity variations. In R. Dmowska, & B. Saltzman (Eds.), *Advances in geophysics*, (Vol. 36, pp. 1–119). Amsterdam, Netherlands: Elsevier.

Forte, A. M., & Perry, H. C. (2000). Geodynamic evidence for a chemically depleted continental tectosphere. *Science*, *290*(5498), 1940–1944. https://doi.org/10.1126/science.290.5498.1940

Forte, A. M., Quéré, S., Moucha, R., Simmons, N. A., Grand, S. P., Mitrovica, J. X., & Rowley, D. B. (2010). Joint seismic-geodynamic-mineral physical modelling of African geodynamics: A reconciliation of deep-mantle convection with surface geophysical constraints. *Earth and Planetary Science Letters*, *295*(3), 329–341. https://doi.org/10.1016/j.epsl.2010.03.017

Forte, A. M., Simmons, N. A., & Grand, S. P. (2015). Constraints on seismic models from other disciplines—Constraints on 3-D seismic models from global geodynamic observables: Implications for the global mantle convective flow. In G. Schubert (Ed.), *Treatise on geophysics*, (2nd ed., Vol. 1, pp. 853–907). Amsterdam, Netherlands: Elsevier.

French, S. W., & Romanowicz, B. A. (2014). Whole-mantle radially anisotropic shear velocity structure from spectral-element waveform tomography. *Geophysical Journal International*, *199*(3), 1303–1327. https://doi.org/10.1093/gji/ggu334

French, S. W., & Romanowicz, B. (2015). Broad plumes rooted at the base of the Earth's mantle beneath major hotspots. *Nature*, *525*(7567), 95–99.

Frost, D. A., & Rost, S. (2014). The P-wave boundary of the large-low shear velocity province beneath the Pacific. *Earth and Planetary Science Letters*, *403*, 380–392. https://doi.org/10.1016/j.epsl.2014.06.046

Gaboret, C., Forte, A. M., & Montagner, J. P. (2003). The unique dynamics of the Pacific hemisphere mantle and its signature on seismic anisotropy. *Earth and Planetary Science Letters*, *208*(3–4), 219–233.

Garcia, R., & Souriau, A. (2000). Amplitude of the core-mantle boundary topography estimated by stochastic analysis of core phases. *Physics of the Earth and Planetary Interiors*, *117*, 345–359.

Garnero, E. J., & McNamara, A. K. (2008). Structure and dynamics of Earth's lower mantle. *Science*, *320*(5876), 626–628. https://doi.org/10.1126/science.1148028

Garnero, E. J., McNamara, A. K., & Shim, S.-H. (2016). Continent-sized anomalous zones with low seismic velocity at the base of Earth's mantle. *Nature Geoscience*, *9*, 481–489. https://doi.org/10.1038/ngeo2733

Ghosh, A., Becker, T. W., & Zhong, S. J. (2010). Effects of lateral viscosity variations on the geoid. *Geophysical Research Letters*, *37*(1).

Glišović, P., & Forte, A. M. (2017). On the deep-mantle origin of the Deccan traps. *Science*, *355*(6325), 613–616. https://doi.org/10.1126/science.aah4390

Glišović, P., Forte, A. M., & Ammann, M. W. (2015). Variations in grain size and viscosity based on vacancy diffusion in minerals, seismic tomography, and geodynamically inferred mantle rheology. *Geophysical Research Letters*, *42*(15), 6278–6286.

Grand, S. P. (1994). Mantle shear structure beneath the Americas and surrounding oceans. *Journal of Geophysical Research: Solid Earth*, *99*(B6), 11,591–11,621. https://doi.org/10.1029/94JB00042

Grand, S. P. (2002). Mantle shear-wave tomography and the fate of subducted slabs. *Philosophical Transactions of the Royal Society of London A: Mathematical, Physical and Engineering Sciences*, *360*(1800), 2475–2491.

Gurnis, M. (1992). Rapid continental subsidence following the initiation and evolution of subduction. *Science*, *255*(5051), 1556–1558. https://doi.org/10.1126/science.255.5051.1556

Hager, B. H. (1984). Subducted slabs and the geoid: Constraints on mantle rheology and flow. *Journal of Geophysical Research: Solid Earth*, *89*(B7), 6003–6015. https://doi.org/10.1029/JB089iB07p06003

Hager, B. H., Clayton, R. W., Richards, M. A., Comer, R. P., & Dziewonski, A. M. (1985). Lower mantle heterogeneity, dynamic topography and the geoid. *Nature*, *313*, 541–545. https://doi.org/10.1038/313541a0

Hager, B. H., & O'Connell, R. J. (1981). A simple global model of plate dynamics and mantle convection. *Journal of Geophysical Research: Solid Earth*, *86*(B6), 4843–4867. https://doi.org/10.1029/JB086iB06p04843

Herring, T. A., Mathews, P. M., & Buffett, B. A. (2002). Modeling of nutation-precession: Very long baseline interferometry results. *Journal of Geophysical Research: Solid Earth*, *107*(B4), ETG 4–1–ETG 4–12. https://doi.org/10.1029/2001JB000165

Hill, R. (1952). The elastic behaviour of a crystalline aggregate. *Proceedings of the Physical Society. Section A*, *65*(5), 349–354.

Hirose, K. (2006). Postperovskite phase transition and its geophysical implications. *Reviews of Geophysics*, *44*, RG3001. https://doi.org/10.1029/2005RG000186

Hofmann, A. W., & Hart, S. R. (1978). An assessment of local and regional isotopic equilibrium in the mantle. *Earth and Planetary Science Letters*, *38*(1), 44–62. https://doi.org/10.1016/0012-821X(78)90125-5

Hwang, Y. K., & Ritsema, J. (2011). Radial Qμ structure of the lower mantle from teleseismic body-wave spectra. *Earth and Planetary Science Letters*, *303*(3–4), 369–375.

Isaak, D. G. (1992). High-temperature elasticity of iron-bearing olivines. *Journal of Geophysical Research: Solid Earth*, *97*(B2), 1871–1885. https://doi.org/10.1029/91JB02675

Ishii, M., & Tromp, J. (1999). Normal-mode and free-air gravity constraints on lateral variations in velocity and density of Earth's mantle. *Science*, *285*(5431), 1231–1236. https://doi.org/10.1126/science.285.5431.1231

Jackson, J. M., Palko, J. W., Andrault, D., Sinogeikin, S. V., Lakshtanov, D. L., Wang, J., & Zha, C.-S. (2003). Thermal expansion of natural orthoenstatite to 1473 K. *European Journal of Mineralogy*, *15*(3), 469–473.

Jackson, J. M., Sinogeikin, S. V., & Bass, J. D. (2007). Sound velocities and single-crystal elasticity of orthoenstatite to 1073 K at ambient pressure. *Physics of the Earth and Planetary Interiors*, *161*(1–2), 1–12.

Jordan, T. H. (1978). Composition and development of the continental tectosphere. *Nature*, *274*(5671), 544–548.

Kajan T. M., Forte, A. M., & Glišović, P. (2018). The impact of geodynamically constrained lateral viscosity variations on convection-related surface observables. *AGU Fall Meeting*, *Abstract #DI24B-23*.

Karato, S.-i., & Karki, B. B. (2001). Origin of lateral variation of seismic wave velocities and density in the deep mantle. *Journal of Geophysical Research: Solid Earth*, *106*(B10), 21,771–21,783. https://doi.org/10.1029/2001JB000214

Katsura, T., Yoneda, A., Yamazaki, D., Yoshino, T., & Ito, E. (2010). Adiabatic temperature profile in the mantle. *Physics of the Earth and Planetary Interiors*, *183*(1), 212–218. https://doi.org/10.1016/j.pepi.2010.07.001

Kawakatsu, H., & Yoshioka, S. (2011). Metastable olivine wedge and deep dry cold slab beneath southwest Japan. *Earth and Planetary Science Letters*, *303*(1), 1–10. https://doi.org/10.1016/j.epsl.2011.01.008

Kido, M., Yuen, D. A., Čadek, O., & Nakakuki, T. (1998). Mantle viscosity derived by genetic algorithm using oceanic geoid and seismic tomography for whole-mantle versus blocked-flow situations. *Physics of the Earth and Planetary Interiors*, *107*(4), 307–326. https://doi.org/10.1016/S0031-9201(98)00077-6

King, S. D., & Masters, G. (1992). An inversion for radial viscosity structure using seismic tomography. *Geophysical Research Letters*, *19*(15), 1551–1554. https://doi.org/10.1029/92GL01700

Koelemeijer, P., Deuss, A., & Ritsema, J. (2017). Density structure of Earth's lowermost mantle from Stoneley mode splitting observations. *Nature Communications*, *8*(1), 1–10. https://doi.org/10.1038/ncomms15241

Kung, J., Li, B., Uchida, T., & Wang, Y. (2005). In-situ elasticity measurement for the unquenchable high-pressure clinopyroxene phase: Implication for the upper mantle. *Geophysical Research Letters*, *32*(1), L01307. https://doi.org/10.1029/2004GL021661

Kuo, C., & Romanowicz, B. (2002). On the resolution of density anomalies in the Earth's mantle using spectral fitting of normal-mode data. *Geophysical Journal International*, *150*(1), 162–179. https://doi.org/10.1046/j.1365-246X.2002.01698.x

Lai, H., Garnero, E. J., Grand, S. P., Porritt, R. W., & Becker, T. W. (2019). Global travel time data set from adaptive empirical wavelet construction. *Geochemistry, Geophysics, Geosystems*, *20*, 2175–2198.

Laske, G., Masters, G., Ma, Z., & Pasyanos, M. (2013). Update on CRUST1. *0-A 1-degree global model of Earth's crust*. Paper presented at the European Geophysical Union General Assembly, European Geophysical Union, Vienna, Austria.

Lau, H. C. P., Mitrovica, J. X., Davis, J. L., Tromp, J., Yang, H.-Y., & Al-Attar, D. (2017). Tidal tomography constrains Earth's deep-mantle buoyancy. *Nature*, *551*(7680), 321–326. https://doi.org/10.1038/nature24452

Lawrence, J. F., & Wysession, M. E. (2006). QLM9: A new radial quality factor (Qμ) model for the lower mantle. *Earth and Planetary Science Letters*, *241*(3–4), 962–971.

Li, B., & Neuville, D. R. (2010). Elasticity of diopside to 8GPa and 1073K and implications for the upper mantle. *Physics of the Earth and Planetary Interiors*, *183*(3), 398–403. https://doi.org/10.1016/j.pepi.2010.08.009

Li, M., McNamara, A. K., & Garnero, E. J. (2014). Chemical complexity of hotspots caused by cycling oceanic crust through mantle reservoirs. *Nature Geoscience*, *7*(5), 366–370.

Lidaka, T., & Suetsugu, D. (1992). Seismological evidence for metastable olivine inside a subducting slab. *Nature*, *356*, 593–595. https://doi.org/10.1038/356593a0

Lithgow-Bertelloni, C., & Gurnis, M. (1997). Cenozoic subsidence and uplift of continents from time-varying dynamic topography. *Geology*, *25*(8), 735–738.

Liu, L. (2015). The ups and downs of North America: Evaluating the role of mantle dynamic topography since the Mesozoic. *Reviews of Geophysics*, *53*(3), 1022–1049. https://doi.org/10.1002/2015RG000489

Liu, L., Spasojević, S., & Gurnis, M. (2008). Reconstructing Farallon plate subduction beneath North America back to the Late Cretaceous. *Science*, *322*(5903), 934–938. https://doi.org/10.1126/science.1162921

Liu, W., Kung, J., Li, B., Nishiyama, N., & Wang, Y. (2009). Elasticity of $(Mg_{0.87}Fe_{0.13})_2SiO_4$ wadsleyite to 12 GPa and 1073 K. *Physics of the Earth and Planetary Interiors*, *174*(1–4), 98–104.

Lu, C., & Grand, S. P. (2016). The effect of subducting slabs in global shear wave tomography. *Geophysical Journal International*, *205*(2), 1074–1085. https://doi.org/10.1093/gji/ggw072

Lu, C., Mao, Z., Lin, J.-F., Zhuravlev, K. K., Tkachev, S. N., & Prakapenka, V. B. (2013). Elasticity of single-crystal iron-bearing pyrope up to 20GPa and 750K. *Earth and Planetary Science Letters*, *361*, 134–142. https://doi.org/10.1016/j.epsl.2012.11.041

Masters, G., Laske, G., Bolton, H., & Dziewonski, A. (2000). The relative behavior of shear velocity, bulk sound speed, and compressional velocity in the mantle: Implications for chemical and thermal structure. In S. i. Karato, A. Forte, R. Liebermann, G. Masters, & L. Stixrude (Eds.), *Earth's deep interior: Mineral physics and tomography from the atomic to the global scale*, (Vol. 177, pp. 63–87). Washington, DC: American Geophysical Union.

Matas, J., & Bukowinski, M. S. T. (2007). On the anelastic contribution to the temperature dependence of lower mantle seismic velocities. *Earth and Planetary Science Letters*, *259*(1), 51–65. https://doi.org/10.1016/j.epsl.2007.04.028

Mathews, P. M., Herring, T. A., & Buffett, B. A. (2002). Modeling of nutation and precession: New nutation series for nonrigid Earth and insights into the Earth's interior. *Journal of Geophysical Research: Solid Earth*, *107*(B4), ETG 3–1–ETG 3–26. https://doi.org/10.1029/2001JB000390

Mitrovica, J. X., & Forte, A. M. (2004). A new inference of mantle viscosity based upon joint inversion of convection and glacial isostatic adjustment data. *Earth and Planetary Science Letters*, *225*(1), 177–189. https://doi.org/10.1016/j.epsl.2004.06.005

Montagner, J.-P., & Kennett, B. (1996). How to reconcile body-wave and normal-mode reference Earth models. *Geophysical Journal International*, *125*(1), 229–248.

Moucha, R., Forte, A. M., Mitrovica, J. X., & Daradich, A. (2007). Lateral variations in mantle rheology: Implications for convection related surface observables and inferred viscosity models. *Geophysical Journal International*, *169*(1), 113–135. https://doi.org/10.1111/j.1365-246X.2006.03225.x

Moucha, R., Forte, A. M., Mitrovica, J. X., Rowley, D. B., Quéré, S., Simmons, N. A., & Grand, S. P. (2008). Dynamic topography and long-term sea-level variations: There is no such thing as a stable continental platform. *Earth and Planetary Science Letters*, *271*(1), 101–108. https://doi.org/10.1016/j.epsl.2008.03.056

Moulik, P., & Ekström, G. (2016). The relationships between large-scale variations in shear velocity, density, and compressional velocity in the Earth's mantle. *Journal of Geophysical Research: Solid Earth*, *121*(4), 2737–2771. https://doi.org/10.1002/2015JB012679

Murakami, M., Ohishi, Y., Hirao, N., & Hirose, K. (2012). A perovskitic lower mantle inferred from high-pressure, high-temperature sound velocity data. *Nature*, *485*(7396), 90–94. https://doi.org/10.1038/nature11004

Murakami, M., Sinogeikin, S. V., Hellwig, H., Bass, J. D., & Li, J. (2007). Sound velocity of $MgSiO_3$ perovskite to Mbar pressure. *Earth and Planetary Science Letters*, *256*(1–2), 47–54.

Nakagawa, T., & Tackley, P. J. (2011). Effects of low-viscosity post-perovskite on thermo-chemical mantle convection in a 3-D spherical shell. *Geophysical Research Letters*, *38*, L04309. https://doi.org/10.1029/2010GL046494

Ni, S., Tan, E., Gurnis, M., & Helmberger, D. (2002). Sharp sides to the African superplume. *Science*, *296*(5574), 1850–1852. https://doi.org/10.1126/science.1070698

Paige, C. C., & Saunders, M. A. (1982). LSQR: An algorithm for sparse linear equations and sparse least squares. *ACM Transactions on Mathematical Software (TOMS)*, *8*(1), 43–71.

Panasyuk, S. V., & Hager, B. H. (2000). Inversion for mantle viscosity profiles constrained by dynamic topography and the geoid, and their estimated errors. *Geophysical Journal International*, *143*(3), 821–836.

Ricard, Y., Richards, M., Lithgow-Bertelloni, C., & Le Stunff, Y. (1993). A geodynamic model of mantle density heterogeneity. *Journal of Geophysical Research: Solid Earth*, *98*(B12), 21,895–21,909. https://doi.org/10.1029/93JB02216

Ricard, Y., Vigny, C., & Froidevaux, C. (1989). Mantle heterogeneities, geoid, and plate motion: A Monte Carlo inversion. *Journal of Geophysical Research: Solid Earth*, *94*(B10), 13,739–13,754. https://doi.org/10.1029/JB094iB10p13739

Ritsema, J., Deuss, A., van Heijst, H. J., & Woodhouse, J. H. (2011). S40RTS: A degree-40 shear-velocity model for the mantle from new Rayleigh wave dispersion, teleseismic traveltime and normal-mode splitting function measurements. *Geophysical Journal International*, *184*(3), 1223–1236. https://doi.org/10.1111/j.1365-246X.2010.04884.x

Ritsema, J., van Heijst, H. J., & Woodhouse, J. H. (1999). Complex shear wave velocity structure imaged beneath Africa and Iceland. *Science*, *286*(5446), 1925–1928. https://doi.org/10.1126/science.286.5446.1925

Ritsema, J., van Heijst, H. J., & Woodhouse, J. H. (2004). Global transition zone tomography. *Journal of Geophysical Research: Solid Earth*, *109*(B02302). https://doi.org/10.1029/2003JB002610

Robertson, G., & Woodhouse, J. (1996). Ratio of relative S to P velocity heterogeneity in the lower mantle. *Journal of Geophysical Research: Solid Earth*, *101*(B9), 20,041–20,052. https://doi.org/10.1029/96JB01905

Rowley, D. B., Forte, A. M., Moucha, R., Mitrovica, J. X., Simmons, N. A., & Grand, S. P. (2013). Dynamic topography change of the eastern United States since 3 million years ago. *Science*, *340*(6140), 1560–1563.

Rowley, D. B., Forte, A. M., Rowan, C. J., Glišović, P., Moucha, R., Grand, S. P., & Simmons, N. A. (2016). Kinematics and dynamics of the East Pacific Rise linked to a stable, deep-mantle upwelling. *Science Advances*, *2*(12), e1601107. https://doi.org/10.1126/sciadv.1601107

Rudolph, M. L., Lekić, V., & Lithgow-Bertelloni, C. (2015). Viscosity jump in Earth's mid-mantle. *Science*, *350*(6266), 1349–1352. https://doi.org/10.1126/science.aad1929

Saltzer, R. L., van der Hilst, R. D., & Karason, H. (2001). Comparing P and S wave heterogeneity in the mantle. *Geophysical Research Letters*, *28*(7), 1335–1338. https://doi.org/10.1029/2000GL012339

Schuberth, B. S. A., Bunge, H. P., & Ritsema, J. (2009). Tomographic filtering of high-resolution mantle circulation models: Can seismic heterogeneity be explained by temperature alone? *Geochemistry, Geophysics, Geosystems*, *10*(5), Q05W03. https://doi.org/10.1029/2009GC002401

Shearer, P. M., & Masters, T. G. (1992). Global mapping of topography on the 660-km discontinuity. *Nature*, *355*, 791–796. https://doi.org/10.1038/355791a0

Shephard, G. E., Liu, L., Müller, R. D., & Gurnis, M. (2012). Dynamic topography and anomalously negative residual depth of the Argentine Basin. *Gondwana Research*, *22*(2), 658–663. https://doi.org/10.1016/j.gr.2011.12.005

Simmons, N. A., Forte, A. M., Boschi, L., & Grand, S. P. (2010). GyPSuM: A joint tomographic model of mantle density and seismic wave speeds. *Journal of Geophysical Research: Solid Earth*, *115*(B12), B12310. https://doi.org/10.1029/2010JB007631

Simmons, N. A., Forte, A. M., & Grand, S. P. (2007). Thermochemical structure and dynamics of the African superplume. *Geophysical Research Letters*, *34*(2).

Simmons, N. A., Forte, A. M., & Grand, S. P. (2009). Joint seismic, geodynamic and mineral physical constraints on three-dimensional mantle heterogeneity: Implications for the relative importance of thermal versus compositional heterogeneity. *Geophysical Journal International*, *177*(3), 1284–1304.

Sinogeikin, S. V., & Bass, J. D. (2002a). Elasticity of majorite and a majorite-pyrope solid solution to high pressure: Implications for the transition zone. *Geophysical Research Letters*, *29*(2), 4–1–4-4. https://doi.org/10.1029/2001GL013937

Sinogeikin, S. V., & Bass, J. D. (2002b). Elasticity of pyrope and majorite-pyrope solid solutions to high temperatures. *Earth and Planetary Science Letters*, *203*(1), 549–555.

Sinogeikin, S. V., Bass, J. D., & Katsura, T. (2003). Single-crystal elasticity of ringwoodite to high pressures and high temperatures: Implications for 520 km seismic discontinuity. *Physics of the Earth and Planetary Interiors*, *136*(1–2), 41–66.

Spasojevic, S., Liu, L., & Gurnis, M. (2009). Adjoint models of mantle convection with seismic, plate motion, and stratigraphic constraints: North America since the Late Cretaceous. *Geochemistry, Geophysics, Geosystems*, *10*(5), Q05W02. https://doi.org/10.1029/2008GC002345

Steinberger, B. (2000). Plumes in a convecting mantle: Models and observations for individual hotspots. *Journal of Geophysical Research: Solid Earth*, *105*(B5), 11,127–11,152. https://doi.org/10.1029/1999JB900398

Steinberger, B. (2016). Topography caused by mantle density variations: Observation-based estimates and models derived from tomography and lithosphere thickness. *Geophysical Journal International*, *205*(1), 604–621. https://doi.org/10.1093/gji/ggw040

Steinberger, B., & Calderwood, A. R. (2006). Models of large-scale viscous flow in the Earth's mantle with constraints from mineral physics and surface observations. *Geophysical Journal International*, *167*(3), 1461–1481. https://doi.org/10.1111/j.1365-246X.2006.03131.x

Steinberger, B., & Torsvik, T. H. (2012). A geodynamic model of plumes from the margins of large low shear velocity provinces. *Geochemistry, Geophysics, Geosystems*, *13*(1), Q01W09. https://doi.org/10.1029/2011GC003808

Steinberger, B. M. (1996). Motion of hotspots and changes of the Earth's rotation axis caused by a convecting mantle. (Doctoral Dissertation). Cambridge, MA: Harvard University.

Stixrude, L., & Lithgow-Bertelloni, C. (2012). Geophysics of chemical heterogeneity in the mantle. *Annual Review of Earth and Planetary Sciences*, *40*(1), 569–595. https://doi.org/10.1146/annurev.earth.36.031207.124244

Su, W.-J., & Dziewonski, A. M. (1997). Simultaneous inversion for 3-D variations in shear and bulk velocity in the mantle. *Physics of the Earth and Planetary Interiors*, *100*(1), 135–156. https://doi.org/10.1016/S0031-9201(96)03236-0

Sun, D., & Miller, M. S. (2013). Study of the western edge of the African large low shear velocity province. *Geochemistry, Geophysics, Geosystems*, *14*(8), 3109–3125. https://doi.org/10.1002/ggge.20185

Suzuki, I., Ohtani, E., & Kumazawa, M. (1980). Thermal expansion of modified spinel, β-Mg_2SiO_4. *Journal of Physics of the Earth*, *28*(3), 273–280.

Tapley, B., Ries, J., Bettadpur, S., Chambers, D., Cheng, M., Condi, F., & Poole, S. (2007). The GGM03 mean Earth gravity model from GRACE. Paper presented at the American Geophysical Union Fall Meeting, American Geophysical Union, San Francisco, CA.

Thorne, M. S., Garnero, E. J., & Grand, S. P. (2004). Geographic correlation between hot spots and deep mantle lateral shear-wave velocity gradients. *Physics of the Earth and Planetary Interiors*, *146*(1–2), 47–63.

Torsvik, T. H., Burke, K., Steinberger, B., Webb, S. J., & Ashwal, L. D. (2010). Diamonds sampled by plumes from the core-mantle boundary. *Nature*, *466*(7304), 352–355. https://doi.org/10.1038/nature09216

Trampert, J., Deschamps, F., Resovsky, J., & Yuen, D. (2004). Probabilistic tomography maps chemical heterogeneities throughout the lower mantle. *Science*, *306*(5697), 853–856. https://doi.org/10.1126/science.1101996

Widmer, R., Masters, G., & Gilbert, F. (1991). Spherically symmetric attenuation within the Earth from normal mode data. *Geophysical Journal International*, *104*(3), 541–553.

Yang, J., Lin, J.-F., Jacobsen, S. D., Seymour, N. M., Tkachev, S. N., & Prakapenka, V. B. (2016). Elasticity of ferropericlase and seismic heterogeneity in the Earth's lower mantle. *Journal of Geophysical Research: Solid Earth*, *121*(12), 8488–8500. https://doi.org/10.1002/2016JB013352

Yang, T., & Gurnis, M. (2016). Dynamic topography, gravity and the role of lateral viscosity variations from inversion of global mantle flow. *Geophysical Journal International*, *207*(2), 1186–1202. https://doi.org/10.1093/gji/ggw335

Zha, C.-S., Duffy, T. S., Downs, R. T., Mao, H.-K., & Hemley, R. J. (1998). Brillouin scattering and X-ray diffraction of San Carlos olivine: Direct pressure determination to 32 GPa. *Earth and Planetary Science Letters*, *159*(1), 25–33. https://doi.org/10.1016/S0012-821X(98)00063-6

Zhao, C., Garnero, E. J., McNamara, A. K., Schmerr, N., & Carlson, R. W. (2015). Seismic evidence for a chemically distinct thermochemical reservoir in Earth's deep mantle beneath Hawaii. *Earth and Planetary Science Letters*, *426*, 143–153. https://doi.org/10.1016/j.epsl.2015.06.012